

DELFT UNIVERSITY OF TECHNOLOGY

REPORT 09-10

NUMERICAL METHODS FOR INDUSTRIAL PROBLEMS WITH PHASE  
CHANGES

IBRAHIM, F. J. VERMOLEN, C. VUIK , AND D. HEGEN

ISSN 1389-6520

Reports of the Department of Applied Mathematical Analysis

Delft 2009

Copyright © 2009 by Department of Applied Mathematical Analysis, Delft, The Netherlands.

No part of the Journal may be reproduced, stored in a retrieval system, or transmitted, in any form or by any means, electronic, mechanical, photocopying, recording, or otherwise, without the prior written permission from Department of Applied Mathematical Analysis, Delft University of Technology, The Netherlands.

# NUMERICAL METHODS FOR INDUSTRIAL PROBLEMS WITH PHASE CHANGES

IBRAHIM<sup>1</sup>, F. J. VERMOLEN, C. VUIK, AND D. HEGEN

ABSTRACT. In this report, we present mathematical modeling and numerical solution of a porous media flow system. Propane ( $C_3H_8$ ) is taken as the fluid through a porous medium with a phase change between liquid and gas. The mass balance and the energy balance (along with Darcy's law) are the basic ingredients of the mathematical model. We have used the numerical density-enthalpy method to solve the system by taking density and enthalpy as state variables whereas pressure, temperature, and gas mass fraction are computed by using density-enthalpy phase diagrams. This approach of solving a multiphase fluid system eliminates the requirement of separate sets of equations for various phases and necessitates fewer parametric assumptions.

## 1. INTRODUCTION

In a previous report [6] we described several numerical methods for solving simple fluid systems by using finite elements (standard Galerkin approach and streamline upwind Petrov-Galerkin method). In that report we gave some details about basis functions and building (assembling) of global matrices from their element matrices. We also applied and compared explicit, semi-explicit and fully implicit time integration schemes. In the current report, we will give a mathematical model and numerical solution of a multiphase porous fluid system. A new method called *the numerical density-enthalpy method* is used to solve the system instead of a traditional method (level set, moving grid, or phase field method). The new approach is more physical, it uses only one set of model equations for each phase, and requires fewer parametric and environmental assumptions. For a detailed discussion of these potential advantages of the new approach over traditional methods, we refer to [1, 2, 5].

Before describing the actual problem, we provide some explanation of *density-enthalpy phase diagrams* [1, 2, 5] which have an important role in our solution strategy. Furthermore, it is also relevant to explain characteristics of hyperbolic partial differential equations because such PDEs are part of the mathematical modeling presented in this report.

**1.1. Density-enthalpy phase diagrams.** In this report we are using the mass and the energy balances to model a fluid system. This mathematical model is discretized and solved numerically for variables such as density  $\rho$ , temperature  $T$ , pressure  $P$ , enthalpy  $h$ , gas mass fraction  $X_G$ , etc. We have taken the density ( $\rho$ ) and the enthalpy ( $h$ ) as state variables which means that temperature, pressure and mass fractions for various phases can be computed (directly from  $\rho$  and  $h$ ), once  $\rho$  and  $h$  are determined. The transformation from  $(\rho, h)$  to  $(T, P, X_G)$  is achieved through  $\rho$ - $h$  phase diagrams. In Figure 1, three such diagrams are shown for Propane ( $C_3H_8$ ). In Figure 1(c), liquid and gas phases are labeled as 'L' and 'G' respectively.

---

<sup>1</sup>The author is indebted to HEC, Pakistan and NUFFIC, The Netherlands for their financial and logistic support.

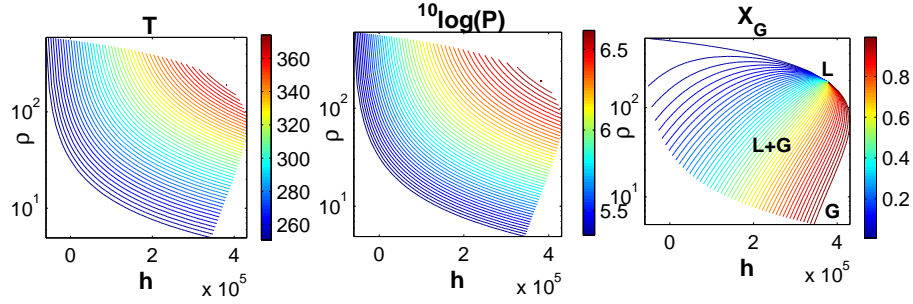


FIGURE 1. (a) Plots of isotherms, (b) isobars, and (c) constant gas mass fraction curves.

The transitional zone (between liquid and gas phases) is marked with 'L+G' which is noticeably larger than the 'L' and 'G' zones.

**1.2. Characteristics of a hyperbolic partial differential equation.** In the next section, a hyperbolic differential equation appears in our mathematical model. The mass conservation law as given in the following equation (along with initial and boundary conditions) can be used to determine a one dimensional mass flow within the fluid system and across the boundaries.

$$\frac{\partial \rho}{\partial t} + \frac{\partial(\rho v)}{\partial x} = 0, \quad x \in [0, L], t > 0. \quad (1)$$

In Figure 2, three sets of characteristics are shown using various velocity profiles. Characteristics shown in Figure 2(b) corresponds to the velocity given in 2(a). Therefore the information (e.g., about  $\rho(x, t)$ ) flows from the left boundary into the system. Hence we are required to specify a boundary condition for  $\rho$  at the left boundary. The information is going out of the system from the right boundary which implies that we do not have to impose a boundary condition for this boundary.

Similarly we specify a boundary condition for  $\rho$  at the right boundary for a case

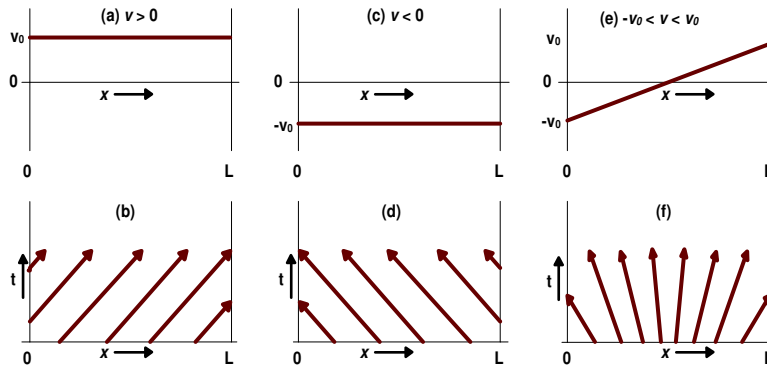


FIGURE 2. Plots of  $\rho$  characteristics using various velocity profiles, (d) information flowing towards right, (e) information flowing towards left, and (f) information is flowing outward from both ends.

as given in Figure 2(c) and (d). In Figure 2(e) and (f), the system is acting as a source, for example due to initial conditions, and the information is going out of the system from both ends. Hence no boundary condition can be imposed in this case.

## 2. ONE-DIMENSIONAL FLUID SYSTEM

Let us consider a one-dimensional fluid (Propane) through a porous medium which experiences phase change. The fluid can appear as a pure liquid or as a pure gas, or as liquid and gas in thermodynamic equilibrium. The domain of computation is a straight line of length  $L$  along the  $x$ -axis.

**2.1. Mathematical modeling.** The mathematical model considered is given as

$$\frac{\partial \rho}{\partial t} + \frac{\partial(\rho v)}{\partial x} = 0, \quad x \in [0, L], t > 0, \quad (2)$$

$$\frac{\partial(\rho h)}{\partial t} + \frac{\partial(\rho h v)}{\partial x} - \frac{\partial}{\partial x} \left( \lambda \frac{\partial T}{\partial x} \right) = q, \quad x \in [0, L], t > 0, \quad (3)$$

$$v = -\frac{K}{\mu} \frac{\partial P}{\partial x}, \quad x \in [0, L], t > 0. \quad (4)$$

Equation (2) represents mass conservation, (3) energy conservation, and (4) is Darcy's law. We have neglected the gravitational effect because it is not important in our Case Study (potato chips). This negligence can also be justified for advection flow (shallow underground flow etc). For convenience, we name equation (2) *the mass equation* and equation (3) *the energy equation*. The permeability  $K$ , dynamic viscosity  $\mu$ , and heat diffusivity  $\lambda$  are assumed to be constants and  $q$  is a known heat source. Density ( $\rho$ ) and enthalpy ( $h$ ) are taken as state variables. Other variables like temperature ( $T$ ), pressure ( $P$ ), and gas mass fraction ( $X_G$ ) are computed by using the  $\rho$ - $h$  diagram [1]. For a complete list of symbols and their definitions, see Table 3.

Initial conditions are given by

$$\begin{aligned} \rho(x, 0) &= \rho_0(x), & x &\in [0, L], \\ h(x, 0) &= h_0(x), & x &\in [0, L]. \end{aligned} \quad (5)$$

For *the mass equation*, the mass flux across the boundary is proportional to the difference in densities provided that  $\epsilon v < 0$ .

$$\begin{aligned} \rho v &= \epsilon k_m (\rho - \rho_a), \quad t > 0, \quad x \in \{0, L\}, \\ \epsilon &= \begin{cases} 1, & \text{if } x = L, \\ -1, & \text{if } x = 0, \end{cases} \end{aligned} \quad (6)$$

where  $k_m$  is a mass transfer coefficient and  $\rho_a$  is the ambient density. If  $\epsilon v \geq 0$ , no boundary condition is applicable for equation (2) as explained in Section 1.2. For *the energy equation*, the boundary condition corresponds to the energy transportation due to convection and diffusion and it is given by

$$-\lambda \frac{\partial T}{\partial x} + (\rho h) v = \epsilon k_h (T - T_a) + \epsilon h_a k_m (\rho - \rho_a), \quad t > 0, \quad x \in \{0, L\}, \quad (7)$$

where  $k_h$  is a heat transfer coefficient,  $h_a$  is the ambient enthalpy, and  $T_a$  is the ambient temperature. *The mass equation* is hyperbolic in  $\rho$ . Therefore the corresponding boundary condition is used only if the velocity is inwards (i.e., mass flows into the system). In the case when velocity is outwards, we do not use boundary conditions for a hyperbolic differential equation.

## 3. NUMERICAL METHOD

To solve this fluid system we have used the Streamline Upwind Petrov-Galerkin method but we will start with the Standard Galerkin algorithm.

**3.1. Standard Galerkin algorithm for the mass equation.** We discretize the mass equation temporally and obtain the weak formulation by multiplying it by a test function  $\eta(x)$  and integrate over the domain  $\Omega$ .

$$\int_0^L \frac{\rho^\tau(x) - \rho^{\tau-1}(x)}{\Delta t} \eta(x) dx = - \int_0^L \frac{\partial(\rho^\tau(x)v^{\tau-1}(x))}{\partial x} \eta(x) dx, \quad 1 \leq \tau \leq \tau_{max}, \quad (8)$$

where  $\tau$  is a time index and  $\tau_{max} = t_{max}/\Delta t$  and  $t_{max}$  is the total simulation time [seconds] and the time step  $\Delta t$  is explained later. Applying integration by parts to the integral on the right-hand side, we have

$$\begin{aligned} \int_0^L \frac{\rho^\tau(x) - \rho^{\tau-1}(x)}{\Delta t} \eta(x) dx &= \underbrace{\rho^\tau(0) v^{\tau-1}(0) \eta(0)}_{A_1} - \underbrace{\rho^\tau(L) v^{\tau-1}(L) \eta(L)}_{B_1} \\ &\quad + \int_0^L \rho^\tau(x) v^{\tau-1}(x) \frac{d\eta}{dx} dx, \end{aligned} \quad (9)$$

where  $A_1$  and  $B_1$  terms take care of the mass flow across boundaries. Now the density  $\rho^\tau(x)$  is approximated by the following scheme.

$$\rho^\tau(x) \approx \sum_{j=0}^N \rho_j^\tau \phi_j(x), \quad (10)$$

where  $N$  is a number related to number of node points. We have  $N + 1$  nodes and  $N$  elements as a result of the spatial domain discretization. The piecewise linear function  $\phi_i$  is defined as

$$\phi_i(x) = \begin{cases} \frac{x-x_{i-1}}{x_i-x_{i-1}}, & \text{for } x \in [x_{i-1}, x_i], \\ \frac{x-x_{i+1}}{x_i-x_{i+1}}, & \text{for } x \in [x_i, x_{i+1}], \\ 0, & \text{for } x \notin [x_{i-1}, x_{i+1}], \end{cases} \quad (11)$$

$$\phi_0(x) = \begin{cases} \frac{x-x_1}{x_0-x_1}, & \text{for } x \in [x_0, x_1], \\ 0, & \text{for } x \notin [x_0, x_1], \end{cases}$$

$$\phi_N(x) = \begin{cases} \frac{x-x_{N-1}}{x_N-x_{N-1}}, & \text{for } x \in [x_{N-1}, x_N], \\ 0, & \text{for } x \notin [x_{N-1}, x_N]. \end{cases}$$

We discretize all unknown variables by the same way as given in equation (10) and substitute value of  $\rho$  into equation (9) along with  $\eta(x) = \phi_i$ ,  $0 \leq i \leq N$ .

$$\sum_{j=0}^N \left( \int_0^L \phi_i(x) \phi_j(x) dx \right) \frac{\rho_j^\tau - \rho_j^{\tau-1}}{\Delta t} = \sum_{j=0}^N \left( \int_0^L v^{\tau-1} \frac{d\phi_i}{dx} \phi_j dx \right) \rho_j^\tau + \hat{A}_1 + \hat{B}_1, \quad (12)$$

where

$$\hat{A}_1 = \begin{cases} \rho_0^\tau v_0^{\tau-1} \phi_i(0), & \text{if } v_0^{\tau-1} \leq 0, \\ -k_m(\rho_0^\tau - \rho_a) \phi_i(0), & \text{if } v_0^{\tau-1} > 0, \end{cases} \quad (13)$$

and

$$\hat{B}_1 = \begin{cases} -\rho_N^\tau v_N^{\tau-1} \phi_i(L), & \text{if } v_N^{\tau-1} \geq 0, \\ -k_m(\rho_N^\tau - \rho_a) \phi_i(L), & \text{if } v_N^{\tau-1} < 0. \end{cases} \quad (14)$$

We have taken  $\rho$  and  $h$  as implicit (i.e., at current time iteration  $\tau$ ) but other variables like velocity and temperature are taken at the previous time iteration

$\tau - 1$ . Equation (12) actually represents a system of difference equations which can be written in a matrix form:

$$M_1 \frac{\boldsymbol{\rho}^\tau - \boldsymbol{\rho}^{\tau-1}}{\Delta t} = S_1^{\tau-1} \boldsymbol{\rho}^\tau + \mathbf{f}_1^{\tau-1}, \quad 1 \leq \tau \leq \tau_{max}. \quad (15)$$

where  $\boldsymbol{\rho}^\tau$  denotes the density solution vector at time step  $\tau$ . The superscripts of the stiffness matrix  $S_1^{\tau-1}$  and the vector  $\mathbf{f}_1^{\tau-1}$  indicate that their computation is based on variables taken at the previous time step. For each element  $(x_{i-1}, x_i)$ ,  $1 \leq i \leq N$ , we compute element matrices  $M_{1e}$  and  $S_{1e}$  and the element vector  $F_{1e}$  and assemble from them their respective global matrices  $M_1$  and  $S_1$  and the global vector  $F_1$ . They are given as

$$M_{1e} = \frac{\Delta x}{2} \begin{bmatrix} 1 & 0 \\ 0 & 1 \end{bmatrix}, \quad (16)$$

$$S_{1e}^{\tau-1} = \frac{1}{2} \begin{bmatrix} -v_{i-1}^{\tau-1} & -v_i^{\tau-1} \\ v_{i-1}^{\tau-1} & v_i^{\tau-1} \end{bmatrix}. \quad (17)$$

We use Newton-Cotes as numerical integration ( $\int_a^b f(x)dx = \frac{b-a}{2}(f(b) + f(a))$ ) because it is accurate enough, since we use piecewise linear basis functions with a second order accuracy. For  $i = 0$  and  $i = N$ , we also take care of expressions given in (13) and (14) for the boundary nodes. Let  $S^{\tau-1}$  be the matrix assembled from the stiffness element matrix  $S_{1e}^{\tau-1}$ , then  $S_1^{\tau-1}$  is determined in the following way,

$$S_1^{\tau-1} = S^{\tau-1} + \theta, \quad (18)$$

where  $\theta = [\theta_{ij}]_{(N+1) \times (N+1)}$ ,  $0 \leq i, j \leq N$  is given as,

$$\theta_{00} = \begin{cases} v_0^{\tau-1}, & \text{if } v_0^{\tau-1} \leq 0, \\ -k_m, & \text{if } v_0^{\tau-1} > 0, \end{cases} \quad (19)$$

$$\theta_{NN} = \begin{cases} -v_N^{\tau-1}, & \text{if } v_N^{\tau-1} \geq 0, \\ -k_m, & \text{if } v_N^{\tau-1} < 0. \end{cases} \quad (20)$$

All other  $\theta_{ij}$  are zero. The vector  $\mathbf{f}_1^{\tau-1}$  is defined in the following way,

$$\mathbf{f}_1^{\tau-1} = \begin{cases} f_0, & \text{for } i = 0, \\ 0, & \text{for } 1 \leq i \leq N - 1, \\ f_N, & \text{for } i = N, \end{cases} \quad (21)$$

$$f_0 = \begin{cases} 0, & \text{if } v_0^{\tau-1} \leq 0, \\ k_m \rho_a, & \text{if } v_0^{\tau-1} > 0, \end{cases} \quad (22)$$

$$f_N = \begin{cases} 0, & \text{if } v_N^{\tau-1} \geq 0, \\ k_m \rho_a, & \text{if } v_N^{\tau-1} < 0. \end{cases} \quad (23)$$

For the  $i$ th element,  $1 \leq i \leq N$ , global matrices and the global vector are updated as

$$M_{1_{i+j-2, i+k-2}} = M_{1_{i+j-2, i+k-2}} + M_{1_{e_{j,k}}}, \quad j, k = \{1, 2\}, \quad (24)$$

$$S_{1_{i+j-2, i+k-2}} = S_{1_{i+j-2, i+k-2}} + S_{1_{e_{j,k}}}, \quad j, k = \{1, 2\}, \quad (25)$$

$$f_{1_{i+j-2, 1}} = f_{1_{i+j-2, 1}} + f_{1_{e_j}}, \quad j = \{1, 2\}. \quad (26)$$

**3.2. Standard Galerkin Algorithm for *the energy equation*.** The time discretized *energy equation* (by using equation (2)) is given by

$$\frac{s^\tau - s^{\tau-1}}{\Delta t} + \frac{\partial(s^\tau v^{\tau-1})}{\partial x} - \frac{\partial}{\partial x} \left( \lambda \frac{\partial T^{\tau-1}}{\partial x} \right) = q^\tau, \quad (27)$$

where  $s^\tau = \rho^\tau h^\tau$ . Although the energy equation (as given by equation 3) is not a hyperbolic PDE but now that we have discretized it temporally and  $T$  is taken at the previous time step, we will treat it as a hyperbolic differential equation. Therefore we use a boundary condition only if the velocity is inward (i.e., the mass is flowing into the system). We multiply the time discretized *energy equation* by the test function  $\eta(x)$  and integrate over  $\Omega$

$$\begin{aligned} \int_0^L \frac{s^\tau - s^{\tau-1}}{\Delta t} \eta(x) dx &= - \int_0^L \frac{\partial(s^\tau v^{\tau-1})}{\partial x} \eta(x) dx + \int_0^L \frac{\partial}{\partial x} \left( \lambda \frac{\partial T^{\tau-1}}{\partial x} \right) \eta(x) dx \\ &+ \int_0^L q^\tau \eta(x) dx. \end{aligned} \quad (28)$$

Applying integration by parts, we have the following weak formulation

$$\begin{aligned} \int_0^L \frac{s^\tau - s^{\tau-1}}{\Delta t} \eta(x) dx &= \underbrace{(s^\tau(0)v^{\tau-1}(0) - \lambda \frac{\partial T^{\tau-1}}{\partial x} |_{x=0}) \eta(0)}_{A_2} \\ &+ \underbrace{(-s^\tau(L)v^{\tau-1}(L) + \lambda \frac{\partial T^{\tau-1}}{\partial x} |_{x=L}) \eta(L)}_{B_2} \\ &+ \int_0^L (s^\tau v^{\tau-1}) \frac{d\eta}{dx} dx - \int_0^L \lambda \frac{\partial T^{\tau-1}}{\partial x} \frac{d\eta}{dx} dx + \int_0^L q^\tau \eta dx, \end{aligned} \quad (29)$$

By using the same discretization scheme as we used for *the mass equation*, we have

$$\begin{aligned} \sum_{j=0}^N \left( \int_0^L \phi_i(x) \phi_j(x) dx \right) \frac{s_j^\tau - s_j^{\tau-1}}{\Delta t} &= \sum_{j=0}^N \left( \int_0^L v^{\tau-1} \frac{d\phi_i}{dx} \phi_j dx \right) s_j^\tau \\ &- \int_0^L \lambda \frac{\partial T^{\tau-1}}{\partial x} \frac{d\phi_i}{dx} dx + \int_0^L q \phi_i dx + \hat{A}_2 + \hat{B}_2. \end{aligned} \quad (30)$$

where,

$$\hat{A}_2 = \begin{cases} s_0^\tau v_0^{\tau-1} \phi_i(0) - k_h(T_0^{\tau-1} - T_a) \phi_i(0), & \text{if } v_0^{\tau-1} \leq 0, \\ -h_a k_m(\rho_0^\tau - \rho_a) \phi_i(0) - k_h(T_0^{\tau-1} - T_a), & \text{if } v_0^{\tau-1} > 0, \end{cases} \quad (31)$$

$$\hat{B}_2 = \begin{cases} -s_N^\tau v_N^{\tau-1} \phi_i(L) - k_h(T_N^{\tau-1} - T_a) \phi_i(L), & \text{if } v_N^{\tau-1} \geq 0, \\ -h_a k_m(\rho_N^\tau - \rho_a) \phi_i(L) - k_h(T_N^{\tau-1} - T_a) \phi_i(L), & \text{if } v_N^{\tau-1} < 0. \end{cases} \quad (32)$$

The matrix form of equation (30) is given by the following equation.

$$M_2 \frac{\mathbf{s}^\tau - \mathbf{s}^{\tau-1}}{\Delta t} = S_2^{\tau-1} \mathbf{s}^\tau + \mathbf{f}_2^{\tau-1}, \quad 1 \leq \tau \leq \tau_{max}. \quad (33)$$

The mass matrix  $M_2$  is the same as  $M_1$  while the stiffness matrix  $S_2^{\tau-1}$  is computed as follows

$$S_2^{\tau-1} = S^{\tau-1} + \gamma, \quad (34)$$



where  $S^{\tau-1}$  is the same matrix as explained in the previous section and used in equation (18) whereas  $\gamma = [\gamma_{ij}]_{(N+1) \times (N+1)}$ , and it is defined as

$$\gamma_{00} = \begin{cases} v_0^{\tau-1}, & \text{if } v_0^{\tau-1} \leq 0, \\ 0, & \text{if } v_0^{\tau-1} > 0, \end{cases} \quad (35)$$

$$\gamma_{0j} = 0, \quad \text{for } 1 \leq j \leq N,$$

$$\gamma_{ij} = 0, \quad \text{for } 1 \leq i, j \leq N-1,$$

$$\gamma_{iN} = 0, \quad \text{for } 0 \leq i \leq N-1,$$

$$\gamma_{NN} = \begin{cases} -v_N^{\tau-1}, & \text{if } v_N^{\tau-1} \geq 0, \\ 0, & \text{if } v_N^{\tau-1} < 0, \end{cases} \quad (36)$$

For the  $i$ th element  $(x_{i-1}, x_i)$ ,  $0 \leq i \leq N$ , the element vector  $\mathbf{f}_{2e}^{\tau-1}$  is used to assemble the global vector  $\mathbf{f}_2^{\tau-1}$  and it is given by

$$\mathbf{f}_{2e}^{\tau-1} = \lambda \frac{T_i^{\tau-1} - T_{i-1}^{\tau-1}}{\Delta x} \begin{bmatrix} 1 \\ -1 \end{bmatrix} + \frac{q}{2\Delta x} \begin{bmatrix} 1 \\ 1 \end{bmatrix}. \quad (37)$$

We have taken  $q$  as constant. Let  $\mathbf{f}^{\tau-1}$  be the global vector assembled from the element vector  $\mathbf{f}_{2e}^{\tau-1}$ , then  $\mathbf{f}_2^{\tau-1}$  is determined as follows

$$\mathbf{f}_2^{\tau-1} = \mathbf{f}^{\tau-1} + \mathbf{g}, \quad (38)$$

where  $\mathbf{g}$  is defined as

$$g_0 = \begin{cases} -k_h(T_0^{\tau-1} - T_a), & \text{if } v_0^{\tau-1} \leq 0, \\ -h_a k_m(\rho_0^\tau - \rho_a) - k_h(T_0^{\tau-1} - T_a), & \text{if } v_0^{\tau-1} > 0, \end{cases} \quad (39)$$

$$g_i = 0, \quad \text{for } 1 \leq i \leq N-1, \quad (40)$$

$$g_N = \begin{cases} -k_h(T_N^{\tau-1} - T_a), & \text{if } v_N^{\tau-1} \geq 0, \\ -h_a k_m(\rho_N^\tau - \rho_a) - k_h(T_N^{\tau-1} - T_a), & \text{if } v_N^{\tau-1} < 0. \end{cases} \quad (41)$$

For  $g_0$  and  $g_N$  expressions we have approximated  $\frac{\partial T^{\tau-1}}{\partial x}$  by  $-k_h(T_0^{\tau-1} - T_a)$ , and  $-k_h(T_N^{\tau-1} - T_a)$ , for  $x = 0$  and for  $x = L$ , respectively.

**3.3. Streamline Upwind Petrov-Galerkin method for mass and energy equations.** Convection dominant problems solved with SGA (Standard Galerkin Algorithm) exhibit undesirable numerical oscillations. A common approach to suppress these oscillations is the use of the SUPG (Streamline Upwind Petrov-Galerkin) method, although some accuracy is lost during the process. The mass equation, in our case, is a convection equation and the energy equation could be convection dominant in a case when  $\frac{\partial T}{\partial x}$  is small and a heat source ( $q$ ) equal to zero. To apply the SUPG method, we split  $\eta(x)$  into two parts  $\eta(x) = w(x) + p(x)$ , where  $w(x)$  is the classical test function and  $p(x)$  denotes a correction in order to take care of the upwind behavior [12]. We obtain

$$\begin{aligned} \int_0^L \frac{\rho^\tau - \rho^{\tau-1}}{\Delta t} w(x) dx + \int_0^L \frac{\partial \rho^\tau}{\partial t} p(x) dx = \\ - \int_0^L \frac{\partial(\rho^\tau v^{\tau-1})}{\partial x} w(x) dx - \int_0^L \frac{\partial(\rho^\tau v^{\tau-1})}{\partial x} p(x) dx, \end{aligned} \quad (42)$$

or

$$\begin{aligned} \int_0^L \frac{\rho^\tau - \rho^{\tau-1}}{\Delta t} w(x) dx + \int_0^L \frac{\rho^\tau - \rho^{\tau-1}}{\partial t} p(x) dx = \\ - \int_0^L \frac{\partial(\rho^\tau v^{\tau-1})}{\partial x} w(x) dx - \int_0^L \left\{ \rho^\tau \frac{\partial v^{\tau-1}}{\partial x} + v^{\tau-1} \frac{\partial \rho^\tau}{\partial x} \right\} p(x) dx. \end{aligned} \quad (43)$$

We neglect the term  $\rho^\tau \frac{\partial v^{\tau-1}}{\partial x}$  because the contribution of this term is not significant [5]. By using  $p(x) = \frac{\Delta x}{2} \xi \frac{d\phi_i}{dx}$  and taking  $\xi = \text{sign}(v)$  which corresponds to the classical upwind scheme, the element mass matrix  $M_{3e}$  is given by

$$M_{3e}^{\tau-1} = M_{1e} + \frac{\Delta x}{4} \begin{bmatrix} -\text{sign}(v_{i-1}^{\tau-1}) & -\text{sign}(v_i^{\tau-1}) \\ \text{sign}(v_{i-1}^{\tau-1}) & \text{sign}(v_i^{\tau-1}) \end{bmatrix}, \quad (44)$$

where  $M_{1e}$  is given in equation (16). The element stiffness matrix is given by,

$$S_{3e}^{\tau-1} = S_{1e}^{\tau-1} + \frac{1}{4} (v_{i-1}^{\tau-1} \text{sign}(v_{i-1}^{\tau-1}) + v_i^{\tau-1} \text{sign}(v_i^{\tau-1})) \begin{bmatrix} -1 & 1 \\ 1 & -1 \end{bmatrix}, \quad (45)$$

where  $S_{1e}^{\tau-1}$  is given in equation (17). The element matrices for *the energy equation* are the same as given earlier i.e.,  $M_{4e} = M_{3e}$  and  $S_{4e} = S_{3e}$ . The contribution of the boundary terms is exactly the same as explained in previous sections. The element vector for *the energy equation* is slightly modified and it is given as,

$$\mathbf{f}_{4e} = \mathbf{f}_{2e} + q \frac{\Delta x}{4} (\text{sign}(v_{i-1}^{\tau-1}) + \text{sign}(v_i^{\tau-1})) \begin{bmatrix} -1 \\ 1 \end{bmatrix}. \quad (46)$$

Finally we have the following system of equations (in matrix form) to be solved,

$$(M_3^{\tau-1} - \Delta t S_3) \boldsymbol{\rho}^\tau = M_3^{\tau-1} \boldsymbol{\rho}^{\tau-1} + \Delta t \mathbf{f}_3^{\tau-1}, \quad (47)$$

$$(M_4^{\tau-1} - \Delta t S_4) \mathbf{s}^\tau = M_4^{\tau-1} \mathbf{s}^{\tau-1} + \Delta t \mathbf{f}_4^{\tau-1}, \quad (48)$$

and we have implemented this set of equations in MATLAB. For each iteration ' $\tau$ ', we obtain solution vectors  $\boldsymbol{\rho}$  and  $\mathbf{h}$ . Other solution vectors  $\mathbf{T}$ ,  $\mathbf{P}$ ,  $\mathbf{X}_G$ , and  $\mathbf{v}$  are obtained by using certain library functions (coded in FORTRAN) containing the density-enthalpy phase diagram calculations.

#### 4. TWO DIMENSIONAL FLUID SYSTEM

**4.1. Mathematical modeling for the two-dimensional fluid system.** The domain  $\Omega$  in this case is taken as a unit square and all gradients of system variables are at most two dimensional. Dynamics of the system is given in the following mass and energy balances.

$$\frac{\partial \rho}{\partial t} + \nabla \cdot (\rho \mathbf{v}) = 0, \quad \mathbf{x} \in \Omega, t > 0, \text{ (mass conservation)}, \quad (49)$$

$$\frac{\partial(\rho h)}{\partial t} + \nabla \cdot (\rho h \mathbf{v}) = \nabla \cdot (\lambda \nabla T) + q, \quad \mathbf{x} \in \Omega, t > 0, \text{ (energy conservation)}, \quad (50)$$

$$\mathbf{v} = -\frac{K}{\mu} \nabla P, \quad \text{(Darcy Law)}. \quad (51)$$

The initial conditions are given by

$$\rho(\mathbf{x}, 0) = \rho_0, \quad \mathbf{x} \in \Omega, \quad (52)$$

$$h(\mathbf{x}, 0) = h_0, \quad \mathbf{x} \in \Omega. \quad (53)$$

The following boundary conditions apply to *the mass equation* if mass flows into the system (i.e.,  $\mathbf{v} \cdot \mathbf{n} \leq 0$ )

$$\rho \mathbf{v} \cdot \mathbf{n} = k_m (\rho - \rho_a), t > 0, \mathbf{x} \in \Gamma, \quad (54)$$

where  $\mathbf{n}$  is a unit outward pointing normal vector at the boundary. The boundary condition for *the energy equation* is given as

$$-\lambda \nabla T \cdot \mathbf{n} + (\rho h) \mathbf{v} \cdot \mathbf{n} = k_h (T - T_a) + h_a k_m (\rho - \rho_a), \quad t > 0, \mathbf{x} \in \Gamma. \quad (55)$$

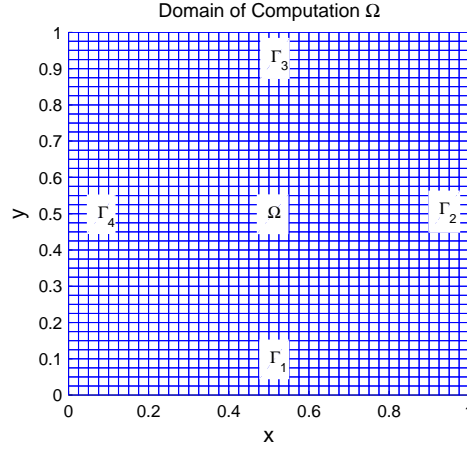


FIGURE 3.

**4.2. Isoparametric transformation.** The domain of computation  $\Omega$  is shown in Figure 3. The interior is marked with  $\Omega$  and the four boundaries are labeled with  $\Gamma_i$ ,  $i = 1, 2, 3, 4$ . At present our numerical computation is limited to a rectangular grid and rectangular elements. In principle we can take any number of nodes along the  $x$ - and the  $y$ -axis. There is no compulsion to take equal number of nodes along both axes. In general we have used a  $41 \times 41$  nodes grid, i.e., the number of nodes along the  $x$ -axis  $N_x$  is 41 and the same number  $N_y$  is true for the  $y$ -axis. Even with  $41 \times 41$  resolution, simulation of 1 second of actual process takes 24 hours of computational time (by using a 2.5 GHz Intel PC, Windows XP, and Matlab). For interior rectangular elements, the number of nodes per element ( $n$ ) is 4 and a lookup table  $E_L$  keeps record of it. For example, the  $k$ th row of  $(E_L)_{N \times n}$  provides information about labels of all 4 nodes of the  $k$ th element, where the total number of elements ( $N$ ) equals  $(N_x - 1)(N_y - 1)$ . Each boundary element  $e_\Gamma$  consists of 2 nodes and its length is denoted by  $L$

$$L = \begin{cases} \Delta x & \text{for } e_\Gamma \in \Gamma_1 \cup \Gamma_3, \\ \Delta y & \text{for } e_\Gamma \in \Gamma_2 \cup \Gamma_4. \end{cases}$$

The node labels for boundary elements for  $\Gamma_i$ ,  $i = 1, 2, 3, 4$ , are kept in lookup tables,  $E_{\Gamma_i}$ ,  $i = 1, 2, 3, 4$ . These lookup tables are also used when we assemble global matrices from their respective element matrices. For example let  $S_e$  be the element matrix for the  $k$ th element,  $k = 1, 2, \dots, N$ , then the corresponding stiffness matrix  $S$  is updated by the following step

$$S_{\alpha,\beta} = S_{\alpha,\beta} + S_{e_{ij}}, \quad i, j = 1, \dots, n, \quad (56)$$

where  $\alpha = E_{k,i}$  and  $\beta = E_{k,j}$ . We cannot give a general shape for continuous (conforming) basis functions in case of rectangular elements. Therefore we have used a technique called *Isoparametric Transformation*. Each rectangular element in  $x$ - $y$ -plane is transformed to a unit square reference element in the  $\xi$ - $\eta$ -plane. Four points  $\mathbf{x}_1$ ,  $\mathbf{x}_2$ ,  $\mathbf{x}_3$ , and  $\mathbf{x}_4$  in each element are transformed to fixed points  $\boldsymbol{\xi}_1$ ,  $\boldsymbol{\xi}_2$ ,  $\boldsymbol{\xi}_3$ , and  $\boldsymbol{\xi}_4$ , where  $\mathbf{x}_i = (x_i, y_i)$  and  $\boldsymbol{\xi}_i = (\xi_i, \eta_i)$ ,  $i = 1, 2, 3, 4$  with  $\boldsymbol{\xi}_i$  are the vertices of the reference element shown in Figure 4. The inverse transformation is given by

$$\mathbf{x} = \sum_{i=1}^4 \mathbf{x}_i \phi_i(\xi, \eta), \quad (57)$$

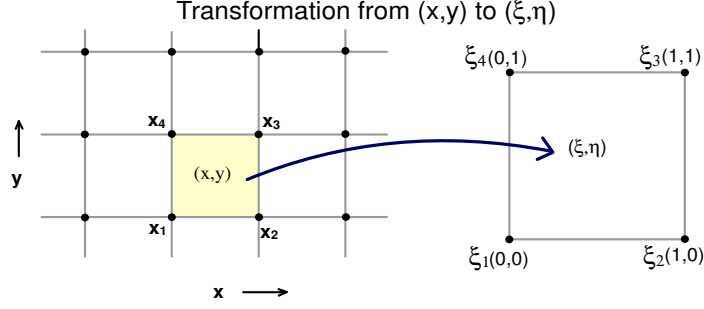


FIGURE 4. Isoparametric transformation from  $(x,y)$  plane to  $(\xi,\eta)$  plane.

where

$$\phi_1 = (1 - \xi)(1 - \eta), \quad \phi_2 = \xi(1 - \eta), \quad \phi_3 = \xi\eta, \quad \text{and} \quad \phi_4 = (1 - \xi)\eta. \quad (58)$$

We need to compute  $\nabla\phi_i(\mathbf{x})$  and  $dx \, dy = \left| \frac{\partial(x,y)}{\partial(\xi,\eta)} \right| d\xi \, d\eta$ , because they appear in certain integral terms arise in computation of element matrices.

$$\text{Let } J = \frac{\partial(x,y)}{\partial(\xi,\eta)} = \begin{bmatrix} \frac{\partial x}{\partial \xi} & \frac{\partial x}{\partial \eta} \\ \frac{\partial y}{\partial \xi} & \frac{\partial y}{\partial \eta} \end{bmatrix}.$$

From equations (57) and (58), we have

$$\begin{aligned} x &= x_1 + (x_2 - x_1)\xi + (x_4 - x_1)\eta + A_x\xi\eta, \\ y &= y_1 + (y_2 - y_1)\xi + (y_4 - y_1)\eta + A_y\xi\eta, \end{aligned}$$

where,  $A_x = (x_1 - x_2 + x_3 - x_4)$  and  $A_y = (y_1 - y_2 + y_3 - y_4)$ ,

$$\begin{aligned} \frac{\partial x}{\partial \xi} &= x_2 - x_1 + A_x\eta, & \frac{\partial x}{\partial \eta} &= x_4 - x_1 + A_x\xi, \\ \frac{\partial y}{\partial \xi} &= y_2 - y_1 + A_y\eta, & \frac{\partial y}{\partial \eta} &= y_4 - y_1 + A_y\xi. \end{aligned}$$

Let  $\Delta_J$  be the determinant of  $J$ ;

$$\Delta_J = (x_2 - x_1 + A_x\eta)(y_4 - y_1 + A_y\xi) - (x_4 - x_1 + A_x\xi)(y_2 - y_1 + A_y\eta)$$

Thus we have determined  $d(x,y) = |\Delta_J|d(\xi,\eta)$ . For  $\nabla\phi_i$ , we have

$$\nabla\phi_i = \left\langle \frac{\partial\phi_i}{\partial x}, \frac{\partial\phi_i}{\partial y} \right\rangle,$$

where,

$$\frac{\partial\phi_i}{\partial x} = \frac{\partial\phi_i}{\partial \xi} \frac{\partial \xi}{\partial x} + \frac{\partial\phi_i}{\partial \eta} \frac{\partial \eta}{\partial x}, \quad i = 1, 2, 3, 4. \quad (59)$$

Now  $\frac{\partial\phi_i}{\partial \xi}$  and  $\frac{\partial\phi_i}{\partial \eta}$  are determined from equations (58) (see Table 1). For  $\frac{\partial \xi}{\partial x}$  and  $\frac{\partial \eta}{\partial x}$ ,

| i | $\frac{\partial\phi_i}{\partial \xi}$ | $\frac{\partial\phi_i}{\partial \eta}$ |
|---|---------------------------------------|--|
| 1 | $-(1 - \eta)$                         | $-(1 - \xi)$                           |
| 2 | $1 - \eta$                            | $-\xi$                                 |
| 3 | $\eta$                                | $\xi$                                  |
| 4 | $-\eta$                               | $1 - \xi$                              |

TABLE 1. Four basis functions for the standard element and its partial derivatives.

we proceed with the following steps,

$$J^{-1} = \frac{1}{\Delta_J} \begin{bmatrix} \frac{\partial y}{\partial \eta} & -\frac{\partial x}{\partial \eta} \\ -\frac{\partial y}{\partial \xi} & \frac{\partial x}{\partial \xi} \end{bmatrix}. \quad (60)$$

But  $J^{-1}$  is also given by the following expression [6],

$$J^{-1} = \begin{bmatrix} \frac{\partial \xi}{\partial x} & \frac{\partial \xi}{\partial y} \\ \frac{\partial \eta}{\partial x} & \frac{\partial \eta}{\partial y} \end{bmatrix}. \quad (61)$$

Comparing equations (60) and (61), we have,

$$\frac{\partial \xi}{\partial x} = \frac{1}{\Delta_J} \frac{\partial y}{\partial \eta} \text{ and } \frac{\partial \eta}{\partial x} = \frac{-1}{\Delta_J} \frac{\partial y}{\partial \xi},$$

where  $\frac{\partial y}{\partial \eta}$  and  $\frac{\partial y}{\partial \xi}$  are already computed. Similarly,

$$\frac{\partial \phi_i}{\partial y} = \frac{\partial \phi_i}{\partial \xi} \frac{\partial \xi}{\partial y} + \frac{\partial \phi_i}{\partial \eta} \frac{\partial \eta}{\partial y}, \quad i = 1, 2, 3, 4, \quad (62)$$

where  $\frac{\partial \xi}{\partial y} = \frac{-1}{\Delta_J} \frac{\partial x}{\partial \eta}$  and  $\frac{\partial \eta}{\partial y} = \frac{1}{\Delta_J} \frac{\partial x}{\partial \xi}$ . Hence  $\nabla \phi_i$  is completely determined. We have used these values to compute element matrices. It is also important to mention that we are using the following Newton-Cotes quadrature rule (for a rectangle) in order to determine 2D integrals appearing in proceeding subsections.

$$\int_{e_{xy}} I(x, y) dx dy \approx \frac{1}{4} \sum_{i=1}^4 I(x_i, y_i). \quad (63)$$

**4.3. Discretization of the mass equation in 2D with standard Galerkin approach.** In order to get the weak formulation, we discretize equation (49) in time (the Euler backward scheme), multiply it by a test function  $\eta(\mathbf{x})$ , and integrate over  $\Omega$

$$\int_{\Omega} \frac{\rho^\tau - \rho^{\tau-1}}{\Delta t} \eta d\Omega = - \int_{\Omega} \nabla \cdot (\rho^\tau \mathbf{v}^{\tau-1}) \eta d\Omega, \quad 1 \leq \tau \leq \tau_{max}. \quad (64)$$

Using

$$\nabla \cdot (\rho \mathbf{v} \eta) = \eta \nabla \cdot (\rho \mathbf{v}) + \rho \mathbf{v} \cdot \nabla \eta, \quad (65)$$

and the divergence theorem

$$\int_{\Omega} \nabla \cdot \mathbf{F} d\Omega = \int_{\Gamma} \mathbf{F} \cdot \mathbf{n} d\Gamma, \quad (66)$$

in equation (64) we have

$$\int_{\Omega} \frac{\rho^\tau - \rho^{\tau-1}}{\Delta t} \eta d\Omega = - \int_{\Gamma} \rho^\tau \eta \mathbf{v}^{\tau-1} \cdot \mathbf{n} d\Gamma + \int_{\Omega} \rho^\tau \mathbf{v}^{\tau-1} \cdot \nabla \eta d\Omega. \quad (67)$$

We choose a set of basis functions  $\{\phi_i(\mathbf{x})\}_{1 \leq i \leq N_d}$ , where  $N_d$  is the number of mesh nodes for unknowns. The solution is approximated by

$$\rho^\tau(\mathbf{x}) = \sum_{j=1}^{N_d} \rho_j^\tau \phi_j(\mathbf{x}). \quad (68)$$

After substitution in the weak form, and choosing  $\eta(\mathbf{x}) = \phi_i$ , for  $i = 1, \dots, N_d$ , we obtain

$$\sum_{j=1}^{N_d} \frac{\rho_j^\tau - \rho_j^{\tau-1}}{\Delta t} \left( \int_{\Omega} \phi_i \phi_j d\Omega \right) = I_1 + \sum_{j=1}^{N_d} \left( \int_{\Omega} \phi_j \mathbf{v}^{\tau-1} \cdot \nabla \phi_i d\Omega \right) \rho_j^\tau, \quad (69)$$

where

$$I_1 = \begin{cases} -\sum_{j=1}^{N_d} \left( \int_{\Gamma} k_m \phi_i \phi_j d\Gamma \right) \rho_j^\tau + \int_{\Gamma} k_m \phi_i \rho_a d\Gamma & \text{for inward velocity,} \\ -\sum_{j=1}^{N_d} \left( \int_{\Gamma} \phi_i \phi_j \mathbf{v}^{\tau-1} \cdot \mathbf{n} d\Gamma \right) \rho_j^\tau & \text{for outward or zero velocity.} \end{cases} \quad (70)$$

The problem domain is discretized by using bilinear elements [subsection 4.2]. This gives a system of difference equations of the form:

$$M_5 \frac{\boldsymbol{\rho}^\tau - \boldsymbol{\rho}^{\tau-1}}{\Delta t} = S_5^{\tau-1} \boldsymbol{\rho}^\tau + \mathbf{f}_5^{\tau-1}. \quad (71)$$

where the mass matrix  $M_5 = \{M_{5_{ij}}\}$ , for  $i, j \in \{1, \dots, N_d\}$ , is

$$M_{5_{ij}} = \int_{\Omega} \phi_i \phi_j d\Omega, \quad (72)$$

the stiffness matrix  $S_5^{\tau-1} = \{S_{5_{ij}}^{\tau-1}\}$ , for  $i, j \in \{1, \dots, N_d\}$ , is

$$S_{5_{ij}}^{\tau-1} = \int_{\Omega} \phi_j \mathbf{v}^{\tau-1} \cdot \nabla \phi_i d\Omega + I_2, \quad (73)$$

where

$$I_2 = \begin{cases} -\int_{\Gamma} k_m \phi_i \phi_j d\Gamma, & \text{for inward velocity,} \\ -\int_{\Gamma} \phi_i \phi_j \mathbf{v}^{\tau-1} \cdot \mathbf{n} d\Gamma, & \text{for outward or zero velocity,} \end{cases} \quad (74)$$

and the vector  $\mathbf{f}_5^{\tau-1} = \{\mathbf{f}_{5_i}^{\tau-1}\}$ , for  $i \in \{1, \dots, N_d\}$ , is

$$\mathbf{f}_{5_i}^{\tau-1} = \begin{cases} \int_{\Gamma} k_m \phi_i \rho_a d\Gamma, & \text{for inward velocity,} \\ 0, & \text{for outward or zero velocity.} \end{cases} \quad (75)$$

Of course these global matrices and the vector are assembled from their respective element matrices and the element vector, as explained in case of the one-dimensional model.

**Computation of element matrices.** By using equation (72), we can determine the element mass matrix for the  $k$ th element  $e_{xy}$ ,  $k = 1, 2, \dots, N$  ( $N =$  number of elements, whereas  $N_d$  is the number of node points)

$$\begin{aligned} M_{5_{e_{ij}}} &= \int_{e_{xy}} \phi_i \phi_j dx dy, \quad i, j = 1, \dots, n, \\ &= \int_{e_{\xi\eta}} \phi_i \phi_j |\Delta_J| d\xi d\eta, \end{aligned}$$

or

$$M_{1_{e_{ij}}} = \delta_{ij} \frac{|\Delta_{J_j}|}{n} \quad n = 4, \quad i, j = 1, \dots, n, \quad (76)$$

where  $\Delta_{J_j}$  is the determinant of the Jacobian matrix  $J$  computed at  $(x_j, y_j)$ . The element stiffness matrix corresponding to  $S_{2D}$  is given by

$$\begin{aligned} S_{5_{e_{ij}}} &= \int_{e_{xy}} \phi_j \mathbf{v}^{\tau-1} \cdot \nabla \phi_i dx dy, \\ &= \int_{e_{\xi\eta}} \phi_j |\Delta_J| d\xi d\eta \\ &= (\nabla_j \phi_i \cdot \mathbf{v}_j^{\tau-1}) \frac{|\Delta_{J_j}|}{n}, \end{aligned} \quad (77)$$

and  $\nabla_j = \langle \frac{\partial}{\partial x} |_{x=x_j}, \frac{\partial}{\partial y} |_{y=y_j} \rangle$ . Hence the  $S_{5_{e_{ij}}}$  is given as

$$S_{5_{e_{ij}}} = \left( \frac{\partial \phi_i}{\partial x_j} v_{x_j}^{\tau-1} + \frac{\partial \phi_i}{\partial y_j} v_{y_j}^{\tau-1} \right) \frac{|\Delta_{J_j}|}{n}, \quad (78)$$

where  $v_{x_j}^{\tau-1}$  and  $v_{y_j}^{\tau-1}$  are  $x$ - and  $y$ -components of the velocity  $v_j^{\tau-1}$ . The computation of other components of equation (78) are given in the previous subsection (equation (59) and (62)). The  $S_{2D}$  matrix is assembled by using the element matrix  $S_{5_e}$  (for an update procedure, refer to equation (56)). Now the stiffness matrix ( $S_5 = \{S_{5_{ij}}\}_{N \times N}$ ) for the mass equation is given by

$$S_{5_{ij}} = S_{2D_{ij}} + I_{3_{ij}}, \quad i, j = 1, 2, \dots, N. \quad (79)$$

We compute  $I_3$  for all boundary elements at four boundary sections ( $\Gamma_1, \Gamma_2, \Gamma_3$ , and  $\Gamma_4$ ). At  $\Gamma_1$  (refer to Figure 3)

$$I_{3_{ij}} = \begin{cases} \delta_{ij} \frac{\Delta y}{2} v_{y_i}^{\tau-1} & \text{if } v_{y_i}^{\tau-1} \leq 0, \\ -\delta_{ij} k_m \frac{L}{2} & \text{if } v_{y_i}^{\tau-1} > 0, \end{cases} \quad (80)$$

where  $\Delta y$  is the spatial step along  $y$ -axis and  $L$  is the length of the boundary element. At  $\Gamma_2$

$$I_{3_{ij}} = \begin{cases} -\delta_{ij} \frac{\Delta x}{2} v_{x_i}^{\tau-1} & \text{if } v_{x_i}^{\tau-1} \geq 0, \\ -\delta_{ij} k_m \frac{L}{2} & \text{if } v_{x_i}^{\tau-1} < 0. \end{cases} \quad (81)$$

At  $\Gamma_3$

$$I_{3_{ij}} = \begin{cases} -\delta_{ij} \frac{\Delta y}{2} v_{y_i}^{\tau-1} & \text{if } v_{y_i}^{\tau-1} \geq 0, \\ -\delta_{ij} k_m \frac{L}{2} & \text{if } v_{y_i}^{\tau-1} < 0. \end{cases} \quad (82)$$

At  $\Gamma_4$

$$I_{3_{ij}} = \begin{cases} \delta_{ij} \frac{\Delta x}{2} v_{x_i}^{\tau-1} & \text{if } v_{x_i}^{\tau-1} \leq 0, \\ -\delta_{ij} k_m \frac{L}{2} & \text{if } v_{x_i}^{\tau-1} > 0. \end{cases} \quad (83)$$

We use equation (75) to obtain the element vector  $\mathbf{f}_{5_e}^{\tau-1}$ . At  $\Gamma = \Gamma_1 \cup \Gamma_2 \cup \Gamma_3 \cup \Gamma_4$

$$f_{5_{e_i}} = \begin{cases} 0 & \text{if } \mathbf{v} \cdot \mathbf{n} \geq 0, \\ k_m \rho_a \frac{L}{2} & \text{if } \mathbf{v} \cdot \mathbf{n} < 0. \end{cases} \quad (84)$$

The global vector  $\mathbf{f}_5$  is updated after computation of the element vector  $f_{5_{e_i}}$  at every boundary element.

**4.4. Discretization of the energy equation in 2D with standard Galerkin approach.** Taking  $s = \rho h$  and proceeding with the same steps, as mentioned for the mass equation, in order to obtain the weak formulation for the 2D energy equation (equation (50)) we have

$$\frac{s^\tau - s^{\tau-1}}{\Delta t} = \nabla \cdot (s^\tau \mathbf{v}^{\tau-1}) + \nabla \cdot (\lambda \nabla T^{\tau-1}) + q^\tau. \quad (85)$$

The weak form is given by

$$\begin{aligned} \int_{\Omega} \frac{s^\tau - s^{\tau-1}}{\Delta t} \eta d\Omega &= - \int_{\Omega} \nabla \cdot (s^\tau \mathbf{v}^{\tau-1}) \eta d\Omega + \int_{\Omega} \nabla \cdot (\lambda \nabla T^{\tau-1}) \eta d\Omega \\ &\quad + \int_{\Omega} q^\tau \eta d\Omega. \end{aligned} \quad (86)$$

Substituting

$$\int_{\Omega} \nabla \cdot (s \mathbf{v}) \eta d\Omega = - \int_{\Gamma} s \eta \mathbf{v} \cdot \mathbf{n} d\Gamma + \int_{\Omega} s \mathbf{v} \cdot \nabla \eta d\Omega, \quad (87)$$

and

$$\int_{\Omega} \nabla \cdot (\lambda \nabla T) \eta d\Omega = \int_{\Gamma} \lambda \frac{\partial T}{\partial n} \eta d\Gamma - \int_{\Omega} \lambda \nabla T \cdot \nabla \eta d\Omega, \quad (88)$$

into equation (86) we get

$$\begin{aligned} \int_{\Omega} \frac{s^{\tau} - s^{\tau-1}}{\Delta t} \eta d\Omega &= - \int_{\Gamma} s^{\tau} \eta \mathbf{v}^{\tau-1} \cdot \mathbf{n} d\Gamma + \int_{\Omega} s^{\tau} \mathbf{v}^{\tau-1} \cdot \nabla \eta d\Omega + \\ &\int_{\Gamma} \lambda \frac{\partial T^{\tau-1}}{\partial n} \eta d\Gamma - \int_{\Omega} \lambda \nabla T^{\tau-1} \cdot \nabla \eta d\Omega + \int_{\Omega} q^{\tau} \eta d\Omega. \end{aligned} \quad (89)$$

Again, the velocity direction has to be taken care of when we solve this equation numerically. For an inward velocity ( $\mathbf{v} \cdot \mathbf{n} < 0$ ), boundary integrals in equation (89) are written as

$$\begin{aligned} - \int_{\Gamma} s^{\tau} \eta \mathbf{v}^{\tau-1} \cdot \mathbf{n} d\Gamma + \int_{\Gamma} \lambda \frac{\partial T^{\tau-1}}{\partial n} \eta d\Gamma &= - \int_{\Gamma} h_a k_m (\rho^{\tau} - \rho_a) d\Gamma \\ &- \int_{\Gamma} k_h (T^{\tau-1} - T_a) d\Gamma, \end{aligned} \quad (90)$$

where we have used equation (54). For an outward velocity ( $\mathbf{v} \cdot \mathbf{n} > 0$ ), equation (54) is not considered instead the heat flux is used

$$\begin{aligned} - \int_{\Gamma} s^{\tau} \eta \mathbf{v}^{\tau-1} \cdot \mathbf{n} d\Gamma + \int_{\Gamma} \lambda \frac{\partial T^{\tau-1}}{\partial n} \eta d\Gamma &= - \int_{\Gamma} s^{\tau} \eta \mathbf{v}^{\tau-1} \cdot \mathbf{n} d\Gamma \\ &- \int_{\Gamma} k_h (T^{\tau-1} - T_a) d\Gamma, \end{aligned} \quad (91)$$

The system of difference equations corresponding to equation (89) is given as

$$M_6 \frac{\mathbf{s}_6^{\tau} - \mathbf{s}_6^{\tau-1}}{\Delta t} = S_6^{\tau-1} \mathbf{s}^{\tau} + \mathbf{f}_6^{\tau-1}, \quad (92)$$

where  $M_6 = M_5$  and the stiffness matrix  $S_6^{\tau-1}$  for  $i, j \in \{1, \dots, N\}$  is

$$S_{6_{ij}} = S_{2D} + I_{4_{ij}}, \quad (93)$$

and  $I_{4_{ij}}$  is computed for all boundary elements. At  $\Gamma_1$

$$I_{4_{ij}} = \begin{cases} \delta_{ij} \frac{\Delta y}{2} v_{y_i}^{\tau-1} & \text{if } v_{y_i}^{\tau-1} \leq 0, \\ 0 & \text{if } v_{y_i}^{\tau-1} > 0. \end{cases} \quad (94)$$

At  $\Gamma_2$

$$I_{4_{ij}} = \begin{cases} -\delta_{ij} \frac{\Delta x}{2} v_{x_i}^{\tau-1} & \text{if } v_{x_i}^{\tau-1} \geq 0, \\ 0 & \text{if } v_{x_i}^{\tau-1} < 0. \end{cases} \quad (95)$$

At  $\Gamma_3$

$$I_{4_{ij}} = \begin{cases} -\delta_{ij} \frac{\Delta y}{2} v_{y_i}^{\tau-1} & \text{if } v_{y_i}^{\tau-1} \geq 0, \\ 0 & \text{if } v_{y_i}^{\tau-1} < 0. \end{cases} \quad (96)$$

At  $\Gamma_4$

$$I_{4_{ij}} = \begin{cases} \delta_{ij} \frac{\Delta x}{2} v_{x_i}^{\tau-1} & \text{if } v_{x_i}^{\tau-1} \leq 0, \\ 0 & \text{if } v_{x_i}^{\tau-1} > 0. \end{cases} \quad (97)$$

The right-hand side vector  $\mathbf{f}_6^{\tau-1}$ , for  $i \in \{1, \dots, N\}$ , is

$$\mathbf{f}_{6_i}^{\tau-1} = - \int_{\Gamma} k_h (T^{\tau-1} - T_a) \phi_i d\Gamma - \int_{\Omega} \lambda \nabla T^{\tau-1} \cdot \nabla \phi_i d\Omega + \int_{\Omega} q^{\tau} \phi_i d\Omega + I_5, \quad (98)$$

$$I_5 = \begin{cases} 0, & \text{if } \mathbf{v}^{\tau-1} \cdot \mathbf{n} \geq 0, \\ - \int_{\Gamma} k_m h_a (\rho^{\tau} - \rho_a) \phi_i d\Gamma, & \text{if } \mathbf{v}^{\tau-1} \cdot \mathbf{n} < 0. \end{cases} \quad (99)$$

We split the vector  $\mathbf{f}_6^{\tau-1}$  into two parts

$$\mathbf{f}_6^{\tau-1} = f_{2D} + g_{2D}, \quad (100)$$



where  $f_{2D}$  takes care of the inner elements while  $g_{2D}$  corresponds to boundary elements. The element vector pertaining to  $\mathbf{f}_{2D}$  is given as

$$f_{6e_i} = - \int_{e_{xy}} \lambda \nabla T^{\tau-1} \cdot \nabla \phi_i dx dy + \int_{e_{xy}} q^\tau \phi_i dx dy, \quad (101)$$

$$= - \sum_{j=1}^n \sum_{k=1}^n \frac{\lambda}{n} T_k^{\tau-1} \left( \frac{\partial \phi_i}{\partial x_j} \frac{\partial \phi_k}{\partial x_j} + \frac{\partial \phi_i}{\partial y_j} \frac{\partial \phi_k}{\partial y_j} \right) |\Delta J_j| + \frac{1}{n} \sum_{j=1}^n q_j^\tau |\Delta J_j|. \quad (102)$$

The vector  $g_{2D} = \{g_{2D_i}\}_{2N_x+2N_y}$  is determined at boundary nodes. At  $\Gamma$

$$g_{2D_i} = \begin{cases} I_e & \text{if } \mathbf{v}^{\tau-1} \cdot \mathbf{n} \geq 0, \\ -k_m k_h \frac{\Delta x}{2} (\rho_i^\tau - \rho_a) + I_e & \text{if } \mathbf{v}^{\tau-1} \cdot \mathbf{n} < 0, (x, y) \in \Gamma_1 \cup \Gamma_3, \\ -k_m k_h \frac{\Delta y}{2} (\rho_i^\tau - \rho_a) + I_e & \text{if } \mathbf{v}^{\tau-1} \cdot \mathbf{n} < 0, (x, y) \in \Gamma_2 \cup \Gamma_4, \end{cases} \quad (103)$$

where  $I_e$  comes from the first integral on RHS of equation (98) and it is given by

$$I_e = - \int_{e_\Gamma} k_h (T^{\tau-1} - T_a) \phi_i d\Gamma \\ = \begin{cases} -k_h \frac{\Delta x}{2} (T_i^{\tau-1} - T_a), & \text{for } \Gamma_1 \cup \Gamma_3, \\ -k_h \frac{\Delta y}{2} (T_i^{\tau-1} - T_a), & \text{for } \Gamma_2 \cup \Gamma_4. \end{cases} \quad (104)$$

**4.5. The mass equation with SUPG method.** Let us consider equation (64) with  $\eta(\mathbf{x})$  split into two parts  $w$  and  $p$  where  $w$  is the classical test function which ensures the consistency of the scheme and  $P$  denotes a correction term in order to take care of the upwind behavior. We obtain

$$\int_{\Omega} \frac{\rho^\tau - \rho^{\tau-1}}{\Delta t} w d\Omega + \int_{\Omega} \frac{\rho^\tau - \rho^{\tau-1}}{\Delta t} p d\Omega = - \int_{\Omega} \nabla \cdot (\rho^\tau \mathbf{v}^{\tau-1}) w d\Omega \\ - \int_{\Omega} \nabla \cdot (\rho^\tau \mathbf{v}^{\tau-1}) p d\Omega, \quad (105)$$

or

$$\int_{\Omega} \frac{\rho^\tau - \rho^{\tau-1}}{\Delta t} w d\Omega + \int_{\Omega} \frac{\rho^\tau - \rho^{\tau-1}}{\Delta t} p d\Omega = - \int_{\Omega} \nabla \cdot (\rho^\tau \mathbf{v}^{\tau-1}) w d\Omega \\ - \int_{\Omega} \{ \rho^\tau \nabla \cdot \mathbf{v}^{\tau-1} + \mathbf{v}^{\tau-1} \cdot \nabla \rho \} p d\Omega. \quad (106)$$

The first integral on the right-hand side can be written as

$$- \int_{\Omega} \nabla \cdot (\rho^\tau \mathbf{v}^{\tau-1}) w d\Omega = - \int_{\Gamma} \rho^\tau \mathbf{v}^{\tau-1} \cdot \mathbf{n} w d\Gamma + \int_{\Omega} \rho^\tau \mathbf{v}^{\tau-1} \cdot \nabla w d\Omega. \quad (107)$$

We neglect the term  $\rho^\tau \nabla \cdot \mathbf{v}^{\tau-1}$  because it has no significant effect on the numerical results [5]. Now equation (106) can be written as

$$\int_{\Omega} \frac{\rho^\tau - \rho^{\tau-1}}{\Delta t} w d\Omega + \int_{\Omega} \frac{\rho^\tau - \rho^{\tau-1}}{\Delta t} p d\Omega = - \int_{\Gamma} \rho^\tau \mathbf{v}^\tau \cdot \mathbf{n} w d\Gamma + \int_{\Omega} \rho^\tau \mathbf{v}^{\tau-1} \cdot \nabla w d\Omega \\ - \int_{\Omega} (\mathbf{v}^{\tau-1} \cdot \nabla \rho^\tau) p d\Omega. \quad (108)$$

Following the same steps as in SGA method we choose

$$p = \frac{\hbar}{2} \frac{\mathbf{v} \cdot \nabla \phi_i}{\|\mathbf{v}\|}, \quad \|\mathbf{v}\| > 0.$$

We do not have to use SUPG in case of  $\|\mathbf{v}\| = 0$ . The value of  $\hbar$  depends on the direction of the velocity and element dimensions as shown in Figure 5. Its minimum possible value is the length of a side ( $\Delta x$  or  $\Delta y$ ) and the maximum value can be the

diagonal of the rectangular element  $(\sqrt{(\Delta x)^2 + (\Delta y)^2})$ . Using  $p$  we get a system of difference equations of the form

$$M_7^{\tau-1} \frac{\rho^\tau - \rho^{\tau-1}}{\Delta t} = S_7^{\tau-1} \rho^\tau + \mathbf{f}_7^{\tau-1}, \quad (109)$$

where the mass matrix  $M_7^{\tau-1}$ , for  $i, j \in \{1, \dots, N\}$ , is

$$\begin{aligned} M_{7ij}^{\tau-1} &= M_{5ij}^{\tau-1} + \int_{e_{xy}} \left( \frac{\hbar \mathbf{v}^{\tau-1} \cdot \nabla \phi_i}{2 \|\mathbf{v}^{\tau-1}\|} \right) dx dy, \\ &= M_{5ij}^{\tau-1} + \frac{\hbar}{2n |v_{x_j}^{\tau-1}|} \left( \frac{\partial \phi_i}{\partial x_j} v_j^{\tau-1} + \frac{\partial \phi_i}{\partial y_j} v_{y_j}^{\tau-1} \right) |\Delta J_j|. \end{aligned} \quad (110)$$

The stiffness matrix  $S_7^{\tau-1}$ , for  $i, j \in \{1, \dots, N\}$ , is

$$\begin{aligned} S_{7ij}^{\tau-1} &= S_{5ij}^{\tau-1} - \int_{e_{xy}} (\mathbf{v}^{\tau-1} \cdot \nabla \phi_j) \left( \frac{\hbar \mathbf{v}^{\tau-1} \cdot \nabla \phi_i}{2 \|\mathbf{v}^{\tau-1}\|} \right) dx dy, \\ &= S_{5ij}^{\tau-1} - \sum_{k=1}^n \frac{\hbar}{2n} \left( \frac{\partial \phi_j}{\partial x_k} v_{x_k}^{\tau-1} + \frac{\partial \phi_j}{\partial y_k} v_{y_k}^{\tau-1} \right) \left( \frac{\partial \phi_i}{\partial x_k} v_{x_k}^{\tau-1} + \frac{\partial \phi_i}{\partial y_k} v_{y_k}^{\tau-1} \right) \frac{|\Delta J_j|}{|v_k^{\tau-1}|}. \end{aligned} \quad (111)$$

$$(112)$$

and the vector  $\mathbf{f}_7^{\tau-1} = \mathbf{f}_5^{\tau-1}$ .

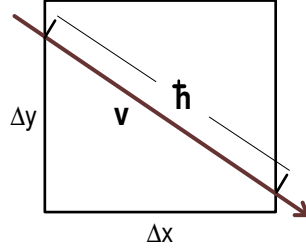


FIGURE 5. The value of  $\hbar$  depends on the direction of the velocity and element dimensions

**4.6. The energy equation with SUPG method.** For the energy equation, we get another system of difference equations of the form

$$M_8^{\tau-1} \frac{\mathbf{s}^\tau - \mathbf{s}^{\tau-1}}{\Delta t} = S_8^{\tau-1} \mathbf{s}^\tau + \mathbf{f}_8^{\tau-1}, \quad (113)$$

where  $M_8^{\tau-1} = M_7^{\tau-1}$  and

$$\begin{aligned} S_{8ij}^{\tau-1} &= S_{6ij}^{\tau-1} - \int_{e_{xy}} (\mathbf{v}^{\tau-1} \cdot \nabla \phi_j) \left( \frac{\hbar \mathbf{v}^{\tau-1} \cdot \nabla \phi_i}{2 \|\mathbf{v}^{\tau-1}\|} \right) dx dy, \\ &= S_{6ij}^{\tau-1} - \sum_{k=1}^n \frac{\hbar}{2n} \left( \frac{\partial \phi_j}{\partial x_k} v_{x_k}^{\tau-1} + \frac{\partial \phi_j}{\partial y_k} v_{y_k}^{\tau-1} \right) \left( \frac{\partial \phi_i}{\partial x_k} v_{x_k}^{\tau-1} + \frac{\partial \phi_i}{\partial y_k} v_{y_k}^{\tau-1} \right) \frac{|\Delta J_j|}{|v_k^{\tau-1}|}, \end{aligned} \quad (114)$$

$$(115)$$

and the vector  $\mathbf{f}_8^{\tau-1}$ , for  $i \in \{1, \dots, N\}$ , is

$$\mathbf{f}_{8i}^{\tau-1} = \mathbf{f}_{6i}^{\tau-1} + \int_{e_{xy}} q_\tau \left( \frac{\hbar \mathbf{v}^{\tau-1} \cdot \nabla \phi_i}{2 \|\mathbf{v}^{\tau-1}\|} \right) dx dy, \quad (116)$$

$$= \mathbf{f}_{6i}^{\tau-1} + \frac{\hbar}{2n} \sum_{j=1}^n q_j^\tau \left( \frac{\partial \phi_i}{\partial x_j} v_{x_j}^{\tau-1} + \frac{\partial \phi_i}{\partial y_j} v_{y_j}^{\tau-1} \right) \frac{|\Delta J_j|}{|v_j^{\tau-1}|} \quad (117)$$

## 5. NUMERICAL EXPERIMENTS

In the following subsections, four different examples (Case Studies) are given.

- Case Study 1: Inwardly insulated system with a positive initial velocity.
- Case Study 2: Inwardly insulated system with an inward initial velocity.
- Case Study 3: Open system, mass and energy flowing into the system.
- Case Study 4: Open system, mass and energy flowing out of the system.

The study of each case consists of 1D numerical results and their explanations. We have compared one of the state variables (i.e., density) for several grid densities at various time instances in order to check for convergence. Finally, the 2D counterpart for each case is also provided. The 2D model is simulated with quadrilateral bilinear elements 4.2. For all numerical experiments, we use the values given in Table 2, for several parameters. Remaining parametric values are given in individual experiments.

**Initial Conditions:** In practice, it is a better choice to mention initial conditions

| Symbol     | value              | comments/units             |
|------------|--------------------|----------------------------|
| $K$        | $10^{-10}$         | $[m^2]$                    |
| $N$        | 40                 | (for 1D, in general)       |
|            | $40 \times 40$     | (for 2D, in general)       |
| $q$        | 0                  | $[W/m^3]$                  |
| $h_a$      | $3.5 \times 10^4$  | (in general) $[J/Kg]$      |
| $\Delta x$ | 0.025              | (in general) $[m]$         |
| $\Delta y$ | 0.025              | (for 2D system) $[m]$      |
| $\Delta t$ | 1/16000            | (with $dx = 0.025$ ) $[s]$ |
| $\mu$      | $5 \times 10^{-5}$ | <i>Pa.s</i>                |
| $\lambda$  | 0.05               | $[W/m/K]$                  |

TABLE 2. Parametric values.

(in our case) in terms of  $(T, X_G)$ , rather than  $(\rho, h)$  because the initial setting of  $T$  and  $X_G$  is easier. Phase diagrams are also available for a transformation from  $(T, X_G)$  to  $(P, \rho, h)$ . Therefore we specify (throughout this report) initial values for  $T$  and  $X_G$  so that initial values for other variables are obtained from them. With a constant  $X_G$ , a linear  $T(0, x)$  with a positive slope results in a nearly linear  $P$  profile with the same slope sign, assuming that difference between minimum and maximum temperature is small (in our numerical experiments, an initial  $\Delta T$  is not greater than 2 [K]). The fluid flows from a higher pressure point to a lower pressure point, therefore we have a negative velocity (from right to left). In Section 5, a desired initial velocity is constructed by choosing a suitable temperature profile. For a positive initial velocity from both boundaries, one option is to set an initial temperature profile as shown in Figure 6(a). Then the resulting initial pressure pattern is depicted in 6(b). Such a pressure profile (a lower pressure at the central part and the higher pressure at and near boundaries) forces an inward initial velocity from both boundaries (see Figure 6(c)).

**5.1. Inwardly insulated system with a positive initial velocity.** We call it an *inwardly insulated system* because the mass and energy can not enter the system but they can flow out of the system in this numerical experiment. We set  $k_m = k_h = 0$  so that no mass or heat is allowed to enter the system. But the mass (and therefore energy) can flow out of the system due to an initial outward velocity at the right boundary ( $v(0, x) > 0$ ). The ambient density and temperature ( $\rho_a$  and  $T_a$ ) do not

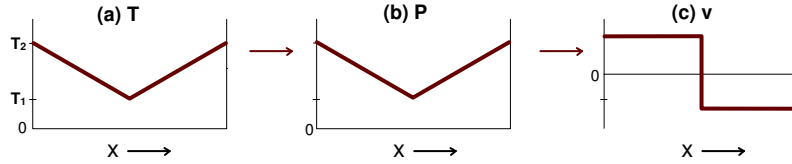


FIGURE 6. (a) Temperature profile for a desired initial condition, (b) the resulting pressure pattern, and (c) an inward velocity resulted from a suitable pressure (indirectly the temperature) profile.

contribute in this example. As can be seen in Figure 7(f), we set an initial positive velocity, from left to right. A desired initial velocity is obtained by setting a suitable initial temperature as explained in Subsection 1.1. Initial conditions are given by

$$\begin{aligned} T(0, x) &= 291 - x, & 0 \leq x \leq 1, \\ X_G(0, x) &= 0.1, & 0 \leq x \leq 1. \end{aligned}$$

A linear temperature results in a linear  $P$ ,  $\rho$ , and  $h$ . A higher pressure value in the left part of the domain, as compared to the right part (Figure 7(d)), forces a positive velocity (Figure 7(f)). The mass cannot enter from the left boundary ( $k_m = 0$ ), therefore, the velocity at the left boundary node goes to zero in a very short time interval. As determined in our numerical experiment, this interval is  $1.56 \times 10^{-5}$  seconds but ideally it should take one iteration (i.e., no time). A positive velocity means that the density in the left side decreases with time (Figure 7(a)). It also means that the mass and the energy are flowing out from the right boundary (refer to equation (20) and 36). A decreasing density in the left side implies that the gas content is increasing as compared to the liquid phase (Figure 7(e)). Figure 8(a) shows that the total mass in the fluid system ( $\int_{\Omega} \rho dx \approx \sum_{i=2}^{N-1} \rho_i^{\tau} \Delta x + \frac{1}{2}(\rho_1^{\tau} \Delta x + \rho_N^{\tau} \Delta)$ ) decreases with time before reaching to a steady-state value. The total energy ( $\int_{\Omega} \rho h dx \approx \sum_{i=2}^{N-1} \rho_i^{\tau} h_i^{\tau} \Delta x + \frac{1}{2}(\rho_1^{\tau} h_1^{\tau} \Delta x + \rho_N^{\tau} h_N^{\tau} \Delta x)$ ) is also shown in Figure 8(b). The total energy decreases because of the outward mass transportation. The mass and energy flow rates are given by [5]

$$\text{mass flow rate} = \sum_{i=1}^{N+1} (S_{3_i}^{\tau-1} \rho_i^{\tau} + f_{3_i}^{\tau-1}), \quad (118)$$

$$\text{energy flow rate} = \sum_{i=1}^{N+1} (S_{4_i}^{\tau-1} s_i^{\tau} + f_{4_i}^{\tau-1}), \quad (119)$$

where  $S_{3_i}^{\tau-1}$  is the  $i$ th column of the stiffness matrix  $S_3^{\tau-1}$  defined in Subsection 3.3. These flow rates (as given in Figure 8(c) and 8(d)) are also used to check for the mass and energy conservation conditions. In accordance with Fourier's law, the temperature (and pressure) decreases in the left part and with the passage of time the temperature (and pressure) gradient decreases (Figure 7(c) and 7(d)). A decreasing pressure gradient lowers the magnitude of the velocity. Both, the mass and heat, flow from left to right, therefore, the total enthalpy also decreases in the left part and increases, relatively, in the right side as shown in Figure 7(b). Apart from the comparison of  $\rho$ ,  $h$ ,  $T$ , and  $P$  values in left and right sides, they always decrease in absolute terms due to the mass outflow. The transport of mass and energy continues until the temperature (and pressure) gradient becomes zero. It is obvious that the temperature and pressure are the main drivers for all transport. Other variables ( $\rho$ ,  $h$ ,  $X_G$ , and  $v$ ) depend on  $T$  and  $P$  whereas  $T$  and  $P$  tend to become constant. The transfer of mass and heat stops as soon the system reaches its steady state value (thermal equilibrium). In Figure 9, a comparison of density

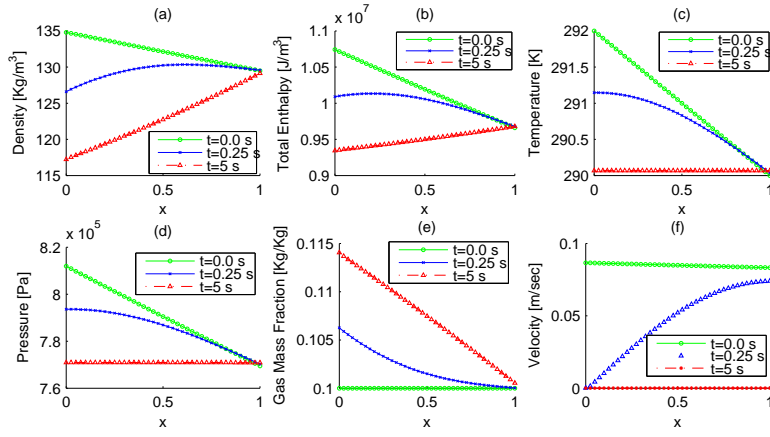


FIGURE 7. Case 1. Inwardly insulated system,  $k_m = 0$ ,  $k_h = 0$ , (a) density, (b) total enthalpy, (c) temperature (d) pressure, (e) gas mass fraction, and (f) velocity.

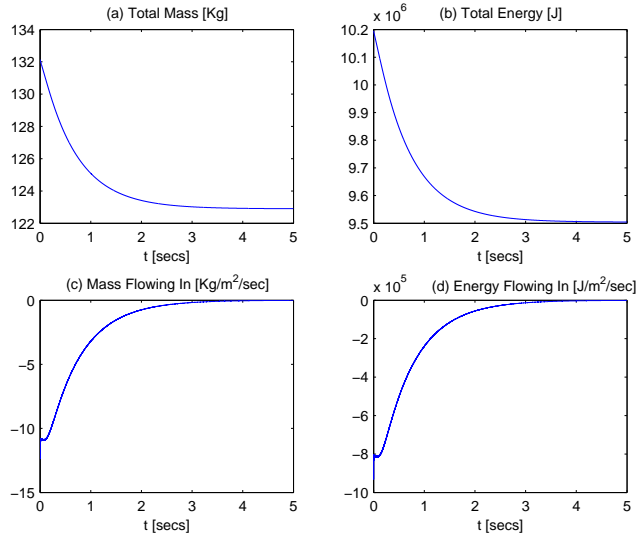


FIGURE 8. Case 1. (a) total mass, (b) total energy, (c) mass flow rate, and (d) energy flow rate.

graphs is given with two grid resolutions (21 and 41 nodes, in other words  $\Delta x = 0.05$  and 0.025). We observe no significant relative difference. The relative difference vector  $\Delta_{rel} = (\Delta_i)_{rel}$ ,  $1 \leq i \leq 21$ , is given by

$$(\Delta_i)_{rel} = \frac{(\rho_i^\tau)_{41} - (\rho_i^\tau)_{21}}{(\rho_i^\tau)_{41}}, (\rho_i^\tau)_{41} > 0. \quad (120)$$

where  $(\rho^\tau)_{41}$  is a density vector determined for a 41 nodes grid, interpolated to a 21 elements vector, so that it could be compared with  $(\rho^\tau)_{21}$ , which is the density vector computed for a 21 nodes grid.

In Figure 10 to 12, we have given simulation results for the 2D model with the same

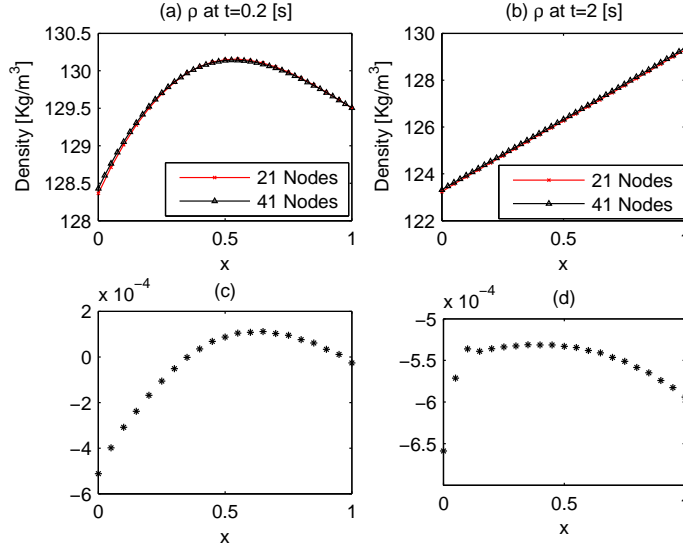


FIGURE 9. Case 1. Inwardly insulated system ( $k_m = 0$ ,  $k_h = 0$ ), density plots with two grid resolutions ( $N = 21$  and  $41$ ). (top row) actual values, (last row) relative difference  $\frac{(\rho_i^\tau)_{41} - (\rho_i^\tau)_{21}}{(\rho_i^\tau)_{41}}$ ,  $1 \leq i \leq 21$ .

boundary conditions along the  $x$ -axis, as we used for the 1D model. i.e.,

$$\begin{aligned} T(0, x, y) &= 291 - x, & 0 \leq x, y \leq 1, \\ X_G(0, x, y) &= 0.1, & 0 \leq x, y \leq 1. \end{aligned} \quad (121)$$

With these initial conditions, the velocity magnitude along  $y$ -axis should be zero throughout the process. But there is a small error as shown in Figure 12, which decreases if we choose higher discretization resolution, spatially and temporally. A comparison for density graphs are given in Figure 13, where cross-sections of 2D density graphs (along the  $x$ -axis) are provided along with 1D graphs for given time instances. There is no significant relative difference  $\left(\frac{(\rho_i^\tau)_{2D} - (\rho_i^\tau)_{1D}}{(\rho_i^\tau)_{2D}}\right)$ ,  $1 \leq i \leq 41$  between the two models for this example.

**5.2. Inwardly insulated system with an inward initial velocity.** In this numerical experiment, again  $k_m = k_h = 0$ , so that  $\rho_a$  and  $T_a$  have no effect on simulation results. Initial conditions are given by

$$\begin{aligned} T(0, x) &= \begin{cases} 291 - x, & \text{for } 0 \leq x \leq 0.5, \\ 291 + x - 1, & \text{for } 0.5 < x \leq 1, \end{cases} \\ X_G(0, x) &= 0.1, \quad 0 \leq x \leq 1. \end{aligned}$$

By using such a temperature profile, one obtains an inward initial velocity as explained in Subsection 1.1. A piecewise linear  $T$  results in a piecewise linear  $\rho$ ,  $P$ , and  $h$  as shown in Figure 14. Since there is no mass flow across boundaries, the velocity values immediately drop to zero at both boundary nodes (Figure 14(f)). A velocity (i.e., the mass flow) directed from sides to the central part increases the density in the central part (Figure 14(a)). A decrease in the density at both sides means that the gas mass fraction increases there (Figure 14(e)). The temperature (and pressure) also lowers at both sides near boundaries and increases at the central part as depicted in Figure 14(c) and 14(d). These trends in the mass and heat flow

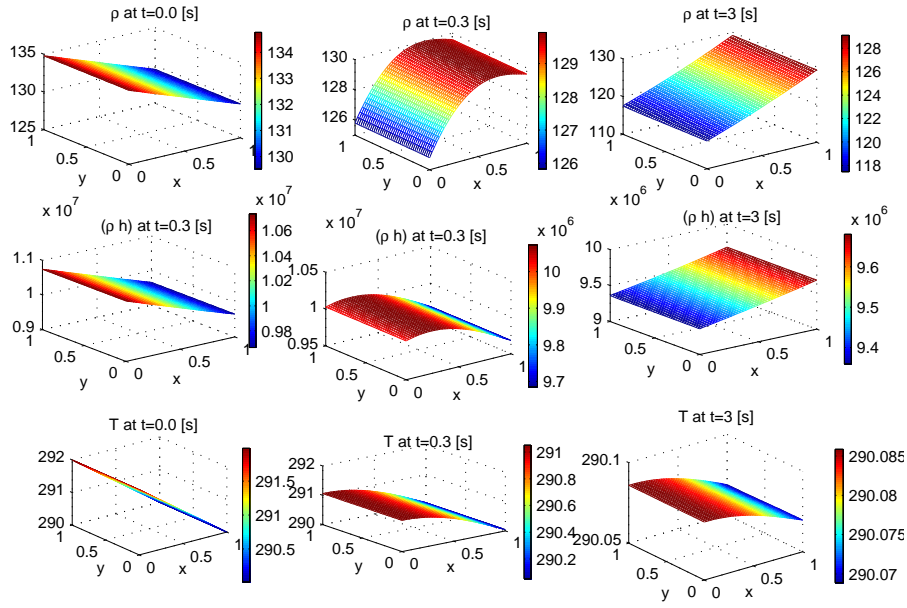


FIGURE 10. Case 1. Inwardly insulated system ( $k_m = 0$ ,  $k_h = 0$ ), 1D conditions, (top row) density [ $kg/m^3$ ] at various time instances (middle row) total enthalpy [ $J/m^3$ ], and (last row) temperature [K].

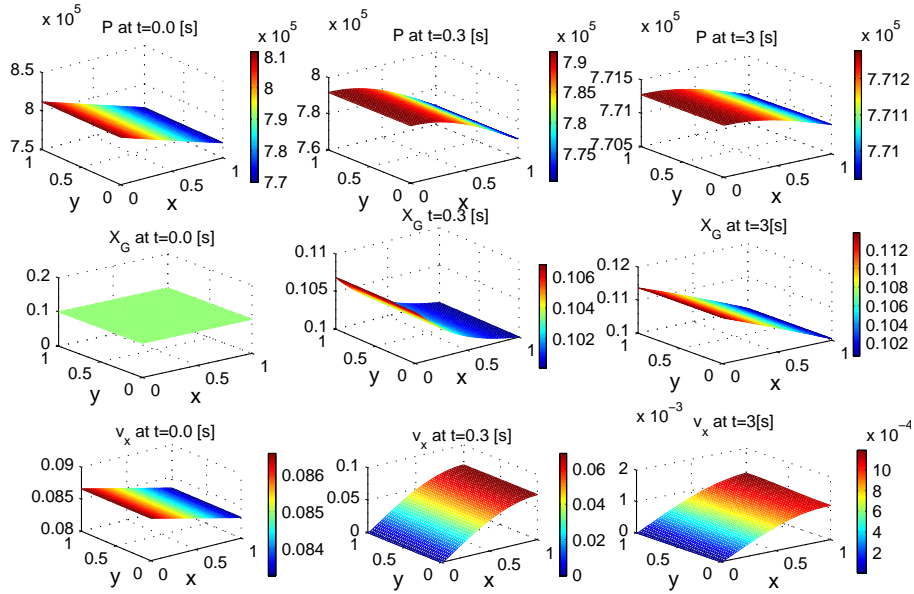


FIGURE 11. Case 1. 1D conditions (top row) pressure [ $Pa$ ] at various time instances (middle row) gas mass fraction [ $kg(gas)/kg(gas + liquid)$ ], and (last row) velocity [ $m/s$ ] in  $x$ -direction.

shape the total enthalpy graphs as given in Figure 14(b). Again all the transportation stops when the temperature and the pressure gradients become zero. In this case, we observe that the steady-state condition is attained in a relatively short time

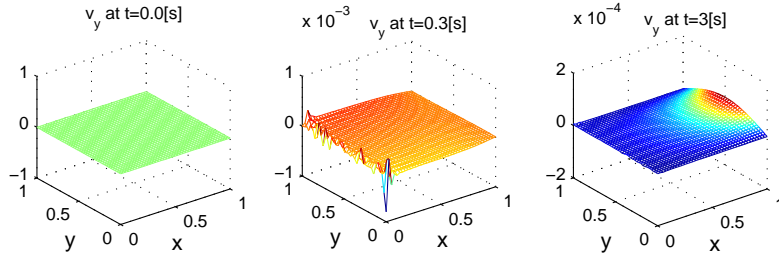


FIGURE 12. Case 1. Velocity [m/s] in  $y$ -direction.

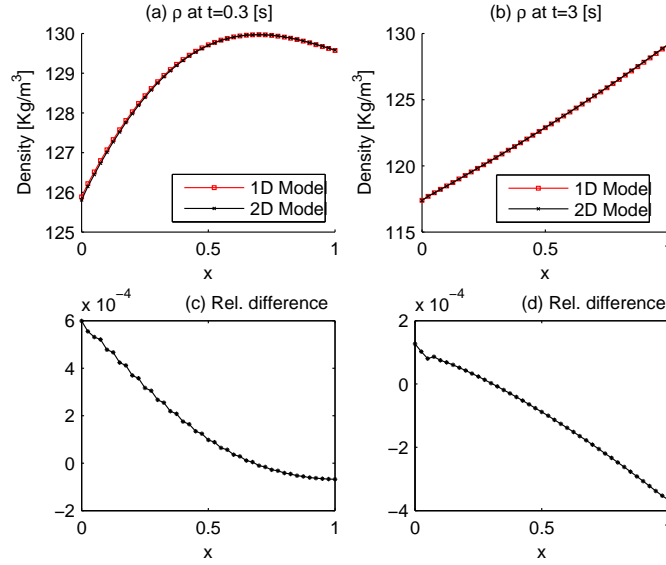


FIGURE 13. Case 1. Inwardly insulated system ( $k_m = 0$ ,  $k_h = 0$ ),  $\Delta x$ , comparison of 1D density plots with graphs taken from cross-section of 2D plots. (Top row) actual density values and (last row) the relative difference  $\frac{(\rho_i^\tau)_{2D} - (\rho_i^\tau)_{1D}}{(\rho_i^\tau)_{2D}}$ ,  $1 \leq i \leq 41$ .

(approx. 0.75 sec). Since there is no mass and the heat transfer across boundaries, the total mass and the total energy of the system should be unchanged with time. But we observe small variations (errors) in the numerical results as shown in Figure Figure 15(a) and 15(b). The dynamic behavior of all variables is similar to 1D case, therefore they have a similar explanation.

In Figure 16, the relative difference is given for two grid resolutions ( $\frac{(\rho_i^\tau)_{41} - (\rho_i^\tau)_{21}}{(\rho_i^\tau)_{41}}$ ,  $1 \leq i \leq 21$ ). In Figure 17 to 19, simulation results for the 2D counterpart of this example are provided.



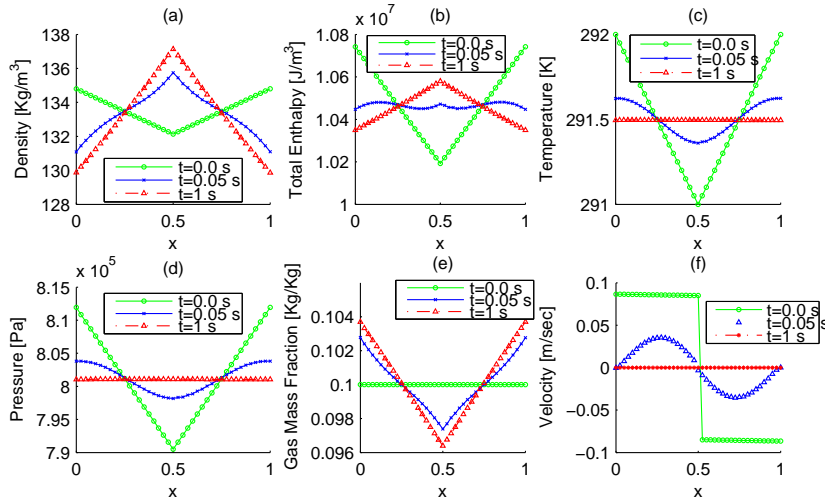


FIGURE 14. Case 2. Inwardly insulated system with an initial inward velocity,  $k_m = 0$ ,  $k_h = 0$ , (a) density, (b) total enthalpy, (c) temperature (d) pressure, (e) gas mass fraction, and (f) velocity.

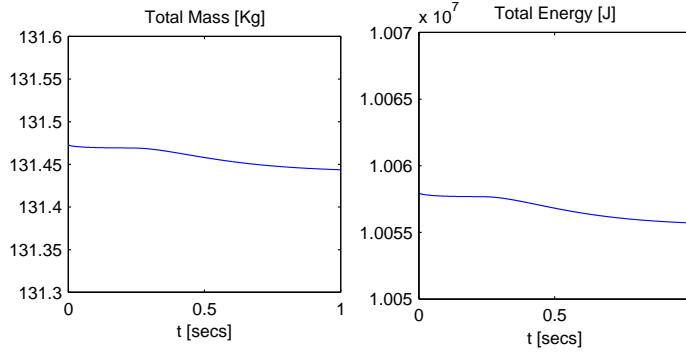


FIGURE 15. Case 2. (a) total mass and (b) total energy in the system.

**5.3. Open System, mass and energy flowing into the system.** In this example, the following initial and environmental data is used

$$\begin{aligned}
 T(0, x) &= 291, \quad 0 \leq x \leq 1, \\
 X_G(0, x) &= 0.1, \\
 \rho_a &= 200, \\
 T_a &= 293.
 \end{aligned}$$

An inflow is triggered by the conductive heat exchange boundary condition given in equations (39) and (41). Hence the mass and the energy flow into the system from both boundaries. The temperature increases with time and attains a steady-state value equal to the ambient temperature  $T_a$ . The density graphs given in Figure 20(a) reveal that, with an inflow mass, the density increases everywhere within the system. An increase in mass and temperature values results in an increase in the total enthalpy in the system (Figure 20(b)). As soon as the temperature (and pressure) becomes constant and the density value at the boundary equals  $\rho_a$ , the system reaches a steady-state value. To investigate the  $\rho$  values given in Figure

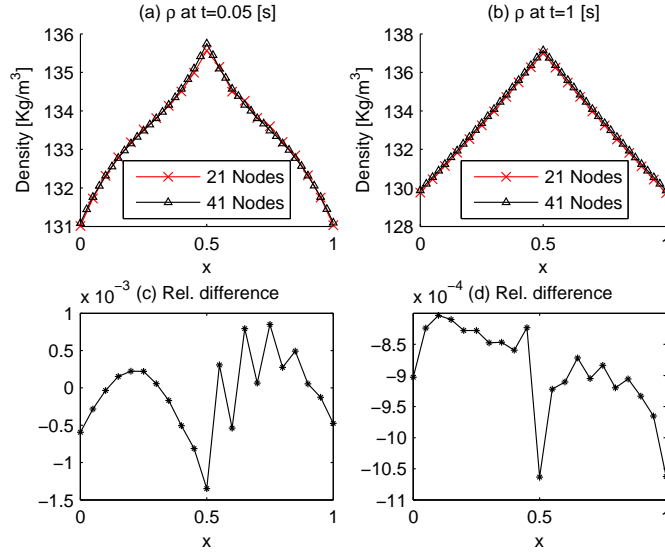


FIGURE 16. Case 2. Inwardly insulated system ( $k_m = 0, k_h = 0$ ), density plots with two grid resolutions ( $N = 21$  and 41). (top row) actual values, (last row) relative difference  $\frac{(\rho_i^T)_{41} - (\rho_i^T)_{21}}{(\rho_i^T)_{41}}$ ,  $1 \leq i \leq 21$ .

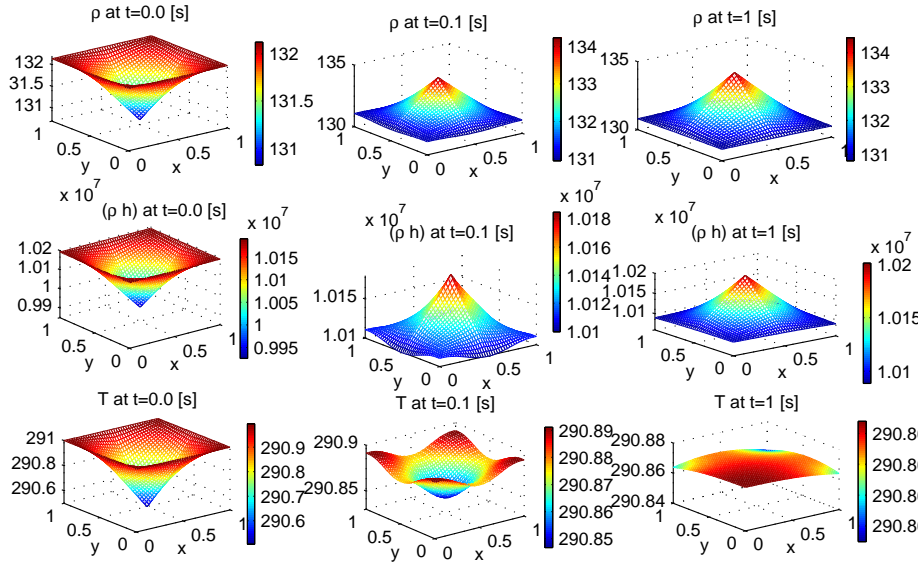


FIGURE 17. Case 2. One-sided insulated system with an initial outwards velocity,  $k_m = 0, k_h = 0$  (top row) density [ $\text{kg/m}^3$ ] at various time instances, (middle row) total enthalpy [ $\text{J/m}^3$ ], and (last row) temperature [ $\text{K}$ ].

20(a) we consider the mass equation

$$\frac{\partial \rho}{\partial t} + \frac{\partial(\rho v)}{\partial x} = 0, \quad x \in [0, L], t > 0, \quad (122)$$

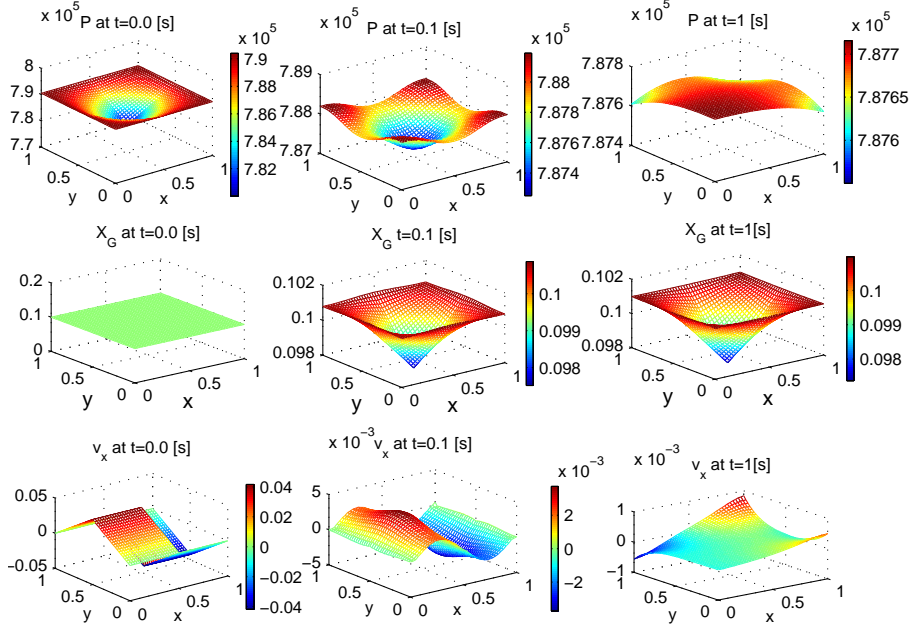


FIGURE 18. Case 2. (top row) pressure [Pa], (middle row) gas mass fraction [ $kg(gas)/kg(gas + liquid)$ ], (last row) velocity [m/s] in  $x$ -direction.

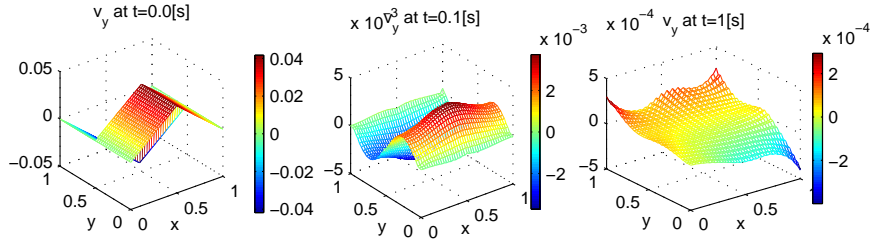


FIGURE 19. Case 2. Velocity [m/s] in  $y$ -direction.

or

$$\frac{\partial \rho}{\partial t} + v \frac{\partial \rho}{\partial x} + \rho \frac{\partial v}{\partial x} = 0, \quad (123)$$

Taking  $x = x(t)$  for  $\rho$  characteristics, we have

$$\frac{\partial \rho}{\partial t} \frac{dt}{dt} + \frac{\partial \rho}{\partial x} \frac{dx}{dt} = -\frac{\partial v}{\partial x} \rho. \quad (124)$$

From the numerical solution, we know that  $\frac{\partial v}{\partial x}$  is negative mostly except that it is zero for  $t = 0$  and for a steady state system. Equation (124) can be written as

$$\frac{d\rho}{dt} = \alpha^2 \rho, \quad (125)$$

where  $\alpha^2 = -\frac{\partial v}{\partial x}$  and the solution for the density is given by,

$$\rho(t) = \rho_0 e^{\int_0^t \alpha^2 dt}. \quad (126)$$

Which indicates that we can expect exponentially increasing behavior in our numerical results. By looking at Figure 20(e) we can also argue that peaks in density

graphs are possibly a result of phase change. But a complete information of density-enthalpy phase diagram's inner mechanism (i.e., relation among variables) is not available. The density graphs comparison with respect to two grid resolutions is

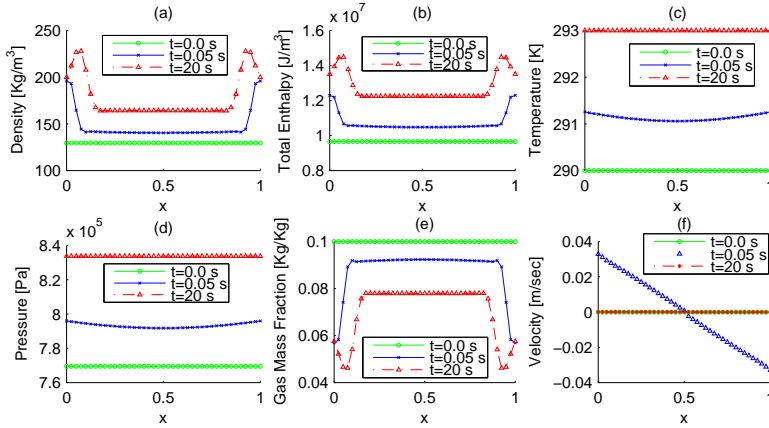


FIGURE 20. Case 3. Open system, mass and energy are flowing into the system  $k_m = 1.5$ ,  $k_h = 10^5$ ,  $\rho_a = 200$ ,  $T_a = 293$  (a) density, (b) total enthalpy, (c) temperature, (d) pressure, (e) gas mass fraction, and (f) velocity.

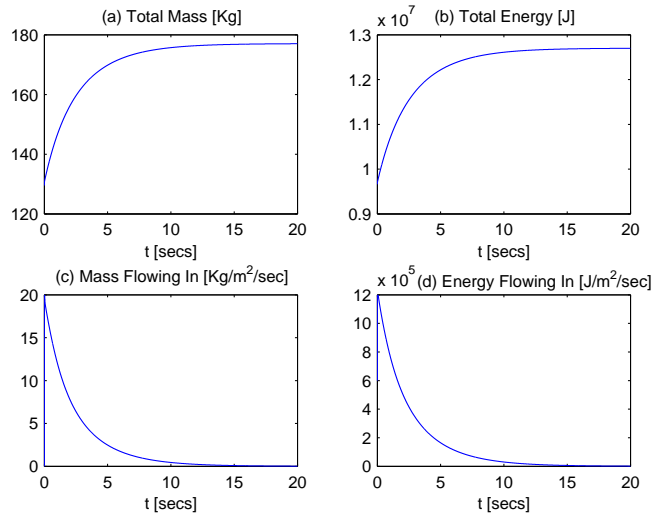


FIGURE 21. Case 3. (a) total mass, (b) total energy, (c) mass flowing into the system, and (d) energy flowing into the system.

given in Figure 22. In this case we observe small differences between these results near boundaries.

The 2D counterpart of this experiment is given in Figure 23 to 25. The explanation for their dynamic behavior is same as given for 1D case.

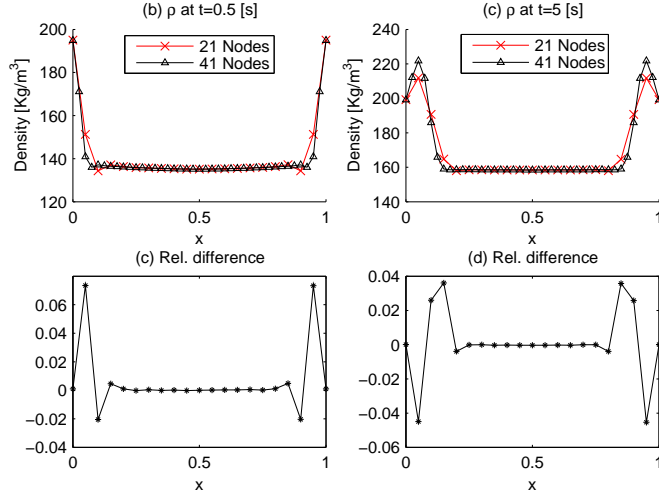


FIGURE 22. Case 3. Open system to mass and heat,  $k_m = 1.5$ ,  $k_h = 10^5$ ,  $\rho_a = 200$ , density plots with two grid resolutions ( $N = 21$  and 41). (top row) actual values, (last row) relative difference,  $\frac{(\rho_i^T)_{41} - (\rho_i^T)_{21}}{(\rho_i^T)_{41}}$ ,  $1 \leq i \leq 21$ .

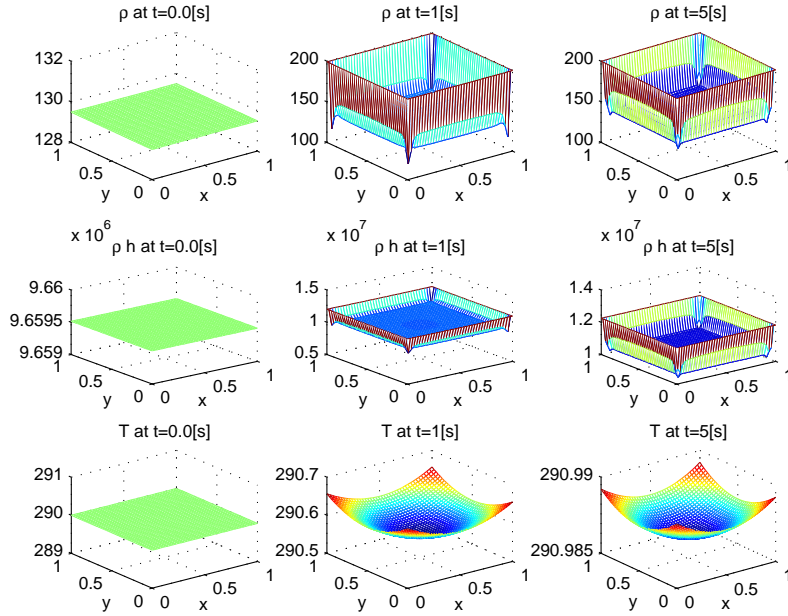


FIGURE 23. Case 3. Open system, mass and heat flowing into the system  $k_m = 1.5$ ,  $k_h = 10^5$ ,  $\rho_a = 200$ ,  $T_a = 293$ , (top row) density [kg/m<sup>3</sup>] at various time instances, (middle row) total enthalpy [ $J/m^3$ ], (last row) temperature [K].

5.4. **Open system, mass and energy flowing out of the system.** In this case we set initial conditions for the mass and the energy outflow

$$\begin{aligned}
 T(0, x) &= 291, \quad 0 \leq x \leq 1, \\
 X_G(0, x) &= 0.1, \\
 \rho_a &= 200, \\
 T_a &= 290.
 \end{aligned}$$

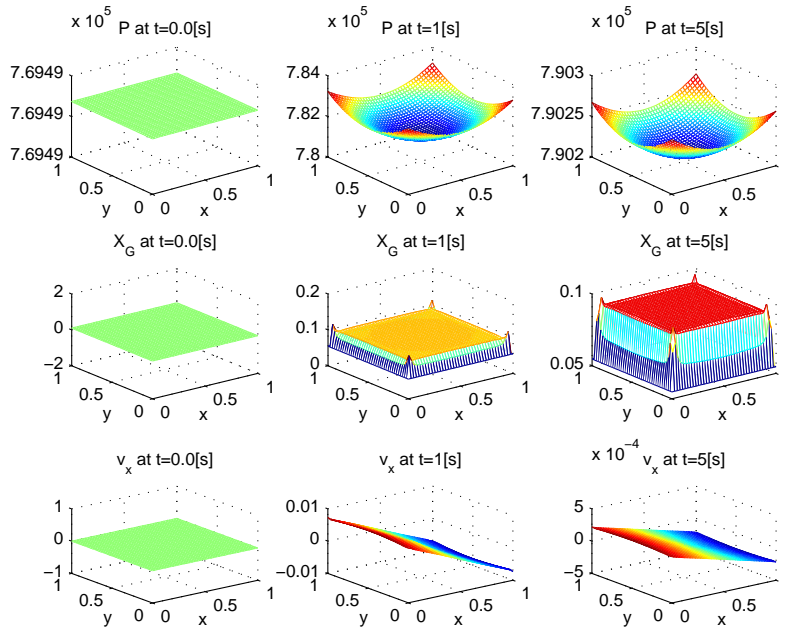


FIGURE 24. Case 3. (top row) pressure [Pa], (middle row) gas mass fraction [Kg of gas/Kg of gas+liquid], (last row) velocity [m/s] in  $x$ -direction.

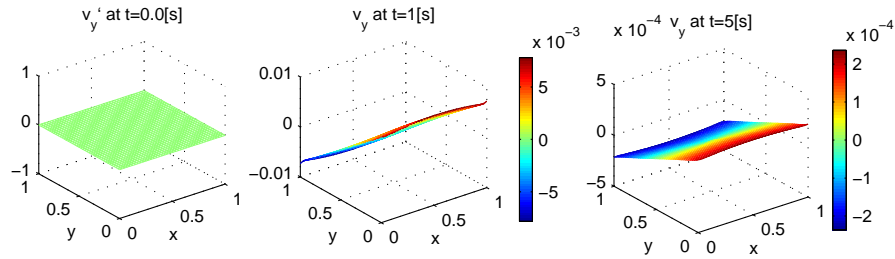


FIGURE 25. Case 3. Velocity [m/s] in  $y$ -direction.

The initial velocity is zero and the flow is triggered by the conductive heat exchange boundary condition given in equations (39) and (41). The mass and the energy is flowing out of the system, therefore density and temperature go down and hence the gas mass fraction increases. For an outward velocity,  $\rho_a$  plays no part. These results are given in Figure 26 and 27. A 'notching effect' can be observed in Figure 26 for density, enthalpy, and gas mass fraction plots, near boundaries. They are not physical and can be minimized by taking higher grid resolutions (as explained later).

In Figure 28 and 29, we have shown a switching effect between different boundary conditions. We know that the system model allows different flow mechanism between velocity conditions  $ev \geq 0$  and  $ev < 0$  as given in discretization sections. If the value of  $v$  is close to zero then a rounding error can cause an undue switching between flow schemes.

The density graphs comparison with respect to several grid resolutions is given in

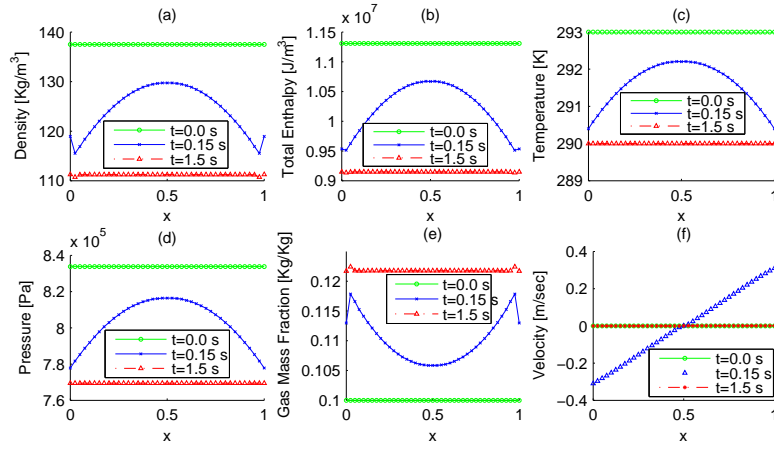


FIGURE 26. Case 4. Open system, mass and energy flowing out of the system,  $k_m = 1.5$ ,  $k_h = 10^5$ ,  $\rho_a = 100$ ,  $T_a = 290$  (a) density, (b) total enthalpy, (c) temperature (d) pressure, (e) gas mass fraction, and (f) velocity.

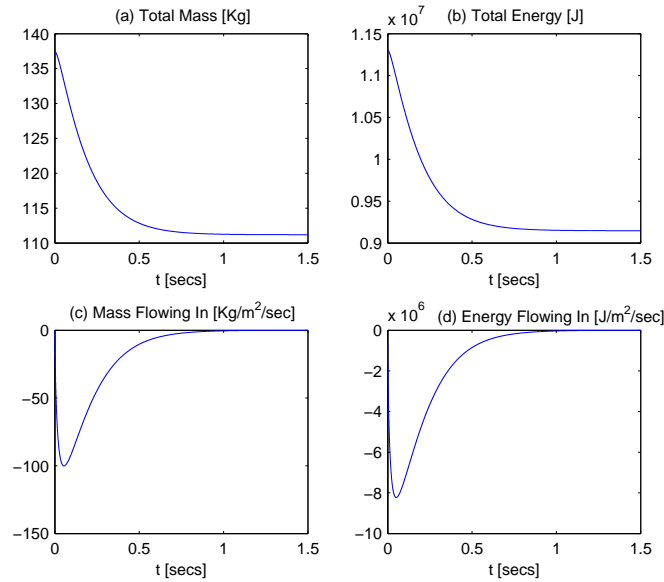


FIGURE 27. Case 4. (a) total mass, (b) total energy, (c) mass flowing into the system, and (d) energy flowing into the system.

Figure 30 which clearly shows a convergence behavior. The density values attain an almost constant steady state condition with 81 nodes. Several plots in Figure 30 show a convergence behavior as we proceed from a low grid (11 nodes) resolution to a higher resolution (81 nodes). We conclude that 'notches' appearing in Figure 26 are not real and they can be avoided by higher resolution grids (or a local grid refinement).

The 2D counterpart of this example is provided in Figure 10 to 33 with a grid resolution  $41 \times 41$ . As seen from Figure 30, we know that this resolution (i.e., 41 nodes) is not enough for accurate results for the current example. Unfortunately it is not possible to obtain higher resolution 2D simulation results at this moment.

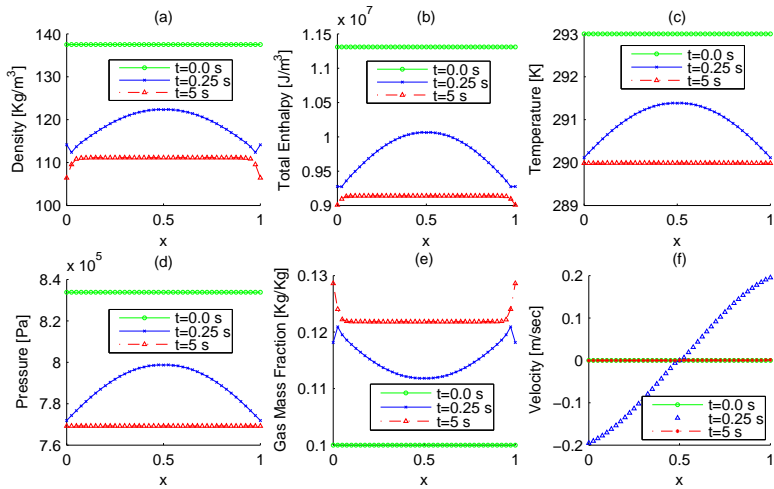


FIGURE 28. Case 4. Open system, mass and energy flowing out of the system, a switching effect due to rounding errors,  $k_m = 1.5$ ,  $k_h = 10^5$ ,  $\rho_a = 100$ ,  $T_a = 290$  (a) density, (b) total enthalpy, (c) temperature (d) pressure, (e) gas mass fraction, and (f) velocity.

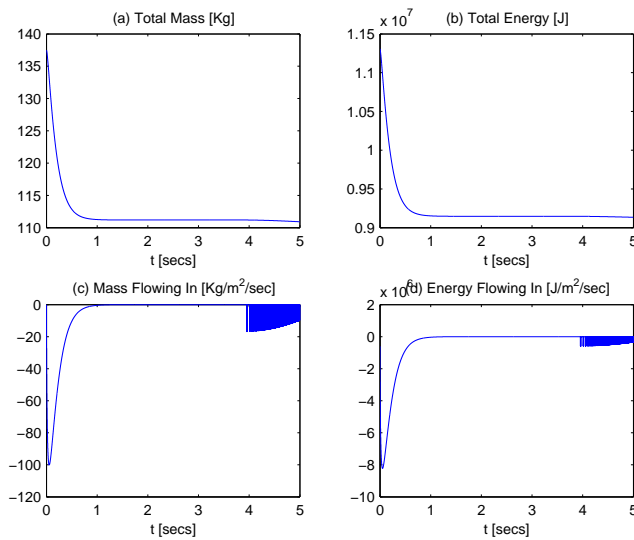


FIGURE 29. Case 4. A switching effect due to rounding errors (a) total mass, (b) total energy, (c) mass flowing into the system, and (d) energy flowing into the system.

## 6. CONCLUSIONS AND FURTHER WORK

It is concluded that the density-enthalpy method can successfully be applied, at least qualitatively, for multi-phase fluid systems where we have certain spatial profiles for system variables.

- 1d and 2d models leads to comparable results for problems with a 1d solution profile.



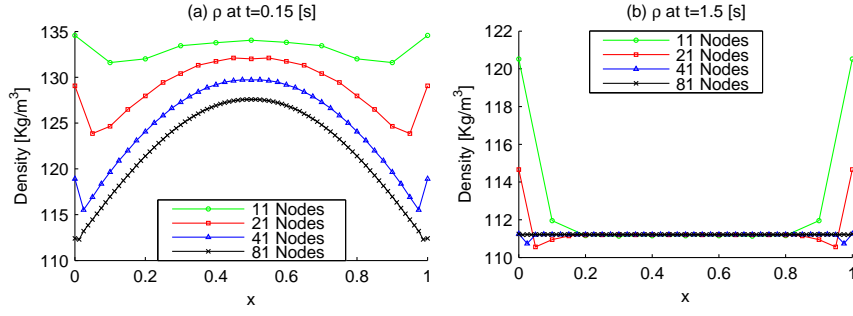


FIGURE 30. Case 4. Open system, mass and heat out of the system, density plots with various grid resolutions,  $k_m = 1.5$ ,  $k_h = 10^5$ ,  $\rho_a = 100$ ,  $T_a = 290$ .

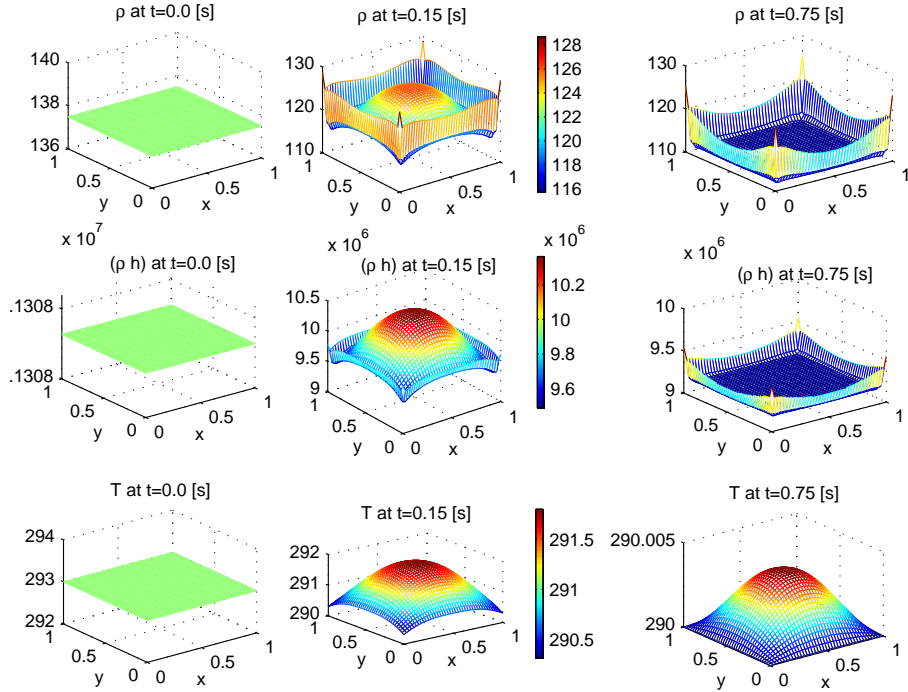


FIGURE 31. Case 4. Open system, mass and heat flowing out of the system  $k_m = 1.5$ ,  $k_h = 10^5$ ,  $\rho_a = 100$ ,  $T_a = 290$  (top row) density at various time instances (middle row) total enthalpy, (last row) temperature.

- For outflow conditions, we do not have a mass transfer coefficient, therefore the mass outflow can not be controlled. Although it also depends on  $T_a$  and  $k_h$ , but in case  $k_h = 0$ , the mass flow depends entirely on the velocity value at the boundary.
- At boundaries, the mass and the heat computations depend on the velocity direction. Rounding error may cause switching between positive and negative velocities and therefore serving as an error source because our model uses different computation schemes for different velocity directions.

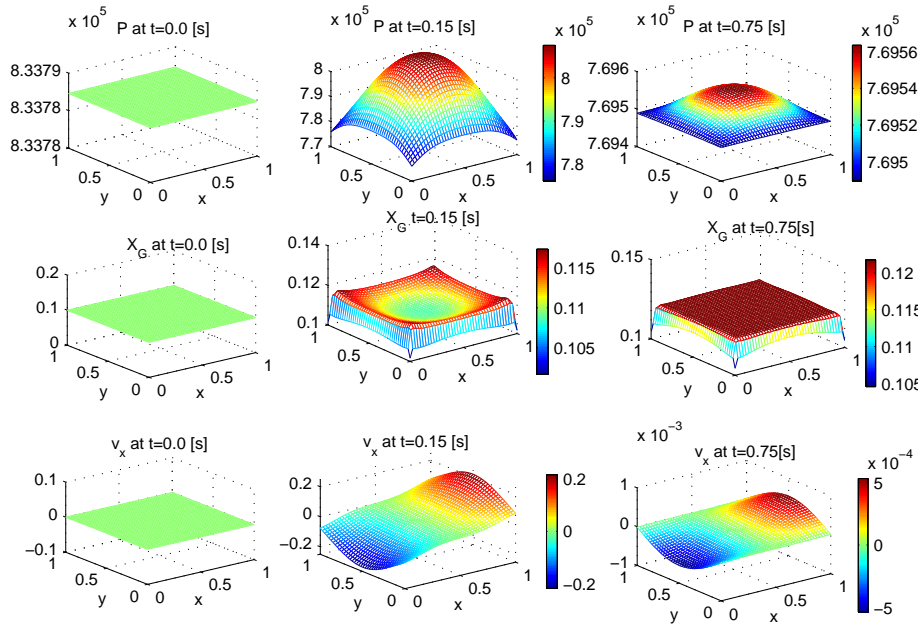


FIGURE 32. Case 4. (top row) pressure, (middle row) gas mass fraction, (last row) velocity in  $x$ -direction.

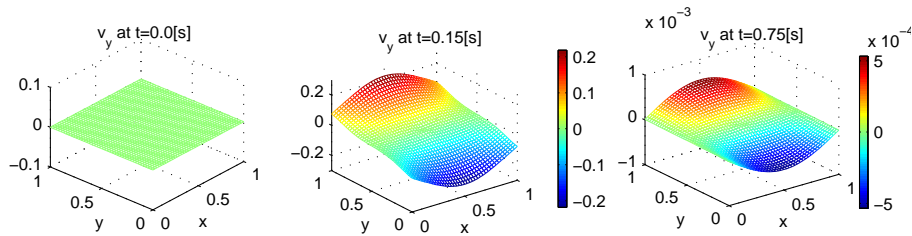


FIGURE 33. Case 4. velocity in  $y$ -direction.

At this moment, the maximum time discretization step  $\Delta t$  is too small, even for a coarse grid. This is a reason for our excessive simulation times and more research needs to be carried out on this topic. An option is to use an adaptive  $\Delta t$  and an adaptive spatial mesh. This is planned for future studies.

#### REFERENCES

- [1] A. R. J. Arendsen, A. I. van Berkel, A. B. M. Heesink, and G. F. Versteeg. Dynamic modelling of thermal processes with phase transitions by means of a density-enthalpy phase diagram. 7th World Congress of Chemical Engineering, Glasgow, Scotland, 2005.
- [2] A. R. J. Arendsen and G. F. Versteeg. Dynamic modelling of refrigeration cycles using density and enthalpy as state variables. 17th International Congress of Chemical and Process Engineering, Prague, The Czech Republic, 2006.
- [3] A. R. J. Arendsen and G. F. Versteeg. Dynamic Thermodynamics with Internal Energy, Volume, and Amount of Moles as States: Application to Liquefied Gas Tank. Ind. Eng. Chem. Res., 2009.
- [4] M. Fabbri and V. R. Voller. The Phase-Field Method in the Sharp-Interface Limit: A comparison between Model Potentials. Journal of Computational Physics, 1997.
- [5] Abdelhaq Abouhafç. Finite Element Modeling Of Thermal Processes With Phase Transitions. Master Thesis, 2007, TUDelft.

|            |                                       |
|------------|---------------------------------------|
| $G$        | gas                                   |
| $h$        | specific enthalpy [ $J/k_g$ ]         |
| $K$        | permeability [ $m^2$ ]                |
| $k_h$      | heat transfer coefficient [ $W/m^2$ ] |
| $k_m$      | mass transfer coefficient [ $m/s$ ]   |
| $L$        | liquid                                |
| $N$        | number of elements                    |
| $P$        | pressure [ $Pa$ ]                     |
| $q$        | heat source [ $W/m^3$ ]               |
| $s$        | total enthalpy $\rho h$ [ $J/m^3$ ]   |
| $T$        | temperature [ $K$ ]                   |
| $T_a$      | ambient temperature $K$               |
| $v$        | velocity [ $m/s$ ]                    |
| $X_G$      | gas mass fraction [ $k_g/k_g$ ]       |
| $\Delta x$ | element length [ $m$ ]                |
| $\Delta t$ | time step [ $s$ ]                     |
| $\mu$      | dynamic viscosity [ $Pa.s$ ]          |
| $\lambda$  | heat conduction [ $W/m/K$ ]           |
| $\rho$     | density [ $Kg/m^3$ ]                  |
| $\rho_a$   | ambient density [ $Kg/m^3$ ]          |
| $\tau$     | time loop index                       |

TABLE 3. Characters and symbols used.

- [6] Ibrahim, C. Vuik, F.J. Vermolen, D. Hegen. Numerical Methods for Industrial Flow Problems. DIAM Reports 08-13, 2008.
- [7] E. Javierre, C. Vuik, F. J. Vermolen, S. van der Zwaag. A comparison of numerical models for one-dimensional Stefan problems. J. Comp. Appl. Math., 2006, 192(2), 445-459.
- [8] Heike Emmerich. The Diffuse Interface Approach in Materials Science, Thermodynamic Concepts and Applications of Phase-Field Models. Springer, Berlin, 2003.
- [9] J.H. Brusche, A. Segal, and C. Vuik. An efficient numerical method for solid-liquid transitions in optical rewritable recording. International Journal for Numerical Methods in Engineering, 77, pp. 702-718, 2009.
- [10] O.C. Zienkiewicz, R.L. Taylor, & J.Z. Zhu, "The Finite Element Method, Its Basis & Fundamentals", 6e, Butterworth-Heinemann, 2005.
- [11] Klaus A. Hoffmann, "Computational Fluid Dynamics, Vol I", 4e, EES, Wichita, USA, 2000.
- [12] J. van Kan, A Segal, F. Vermolen, "Numerical Methods in Scientific Computing", VSSD, 2004.
- [13] Randall J. Leveque, "Finite Volume Methods for Hyperbolic Problems", Cambridge University Press, USA, 2002.
- [14] J.N. Reddy, "An Introduction to the Finite Element Method", 2e, McGraw-Hill, 1993.